

# Seasonal to decadal dynamics of supraglacial lakes on debris-covered glaciers in the Khumbu Region, Nepal

Lucas Zeller<sup>1</sup>, Daniel McGrath<sup>1</sup>, Scott W. McCoy<sup>2</sup>, and Jonathan Jacquet<sup>2</sup>

<sup>1</sup>Department of Geosciences, Colorado State University, Fort Collins, CO 80523, USA

<sup>2</sup>Department of Geological Sciences and Engineering, University of Nevada, Reno, NV 89557, USA

**Correspondence:** Lucas Zeller (Lucas.Zeller@colostate.edu)

**Abstract.** Supraglacial lakes (SGLs) play an important role in debris-covered glacier (DCG) systems by enabling efficient interactions between the subglacial, englacial, and supraglacial environments. Developing a better understanding of the short-term and long-term development of these features is needed to constrain DCG evolution and the hazards posed to downstream communities, ecosystems, and infrastructure from rapid drainage. In this study, we present an analysis of supraglacial lakes on eight DCGs in the Khumbu region of Nepal by automating SGL identification in PlanetScope, Sentinel-2, and Landsat 5-9 images. We identify a regular annual cycle in SGL area, with lakes covering approximately twice as much area during their maximum annual extent (in the pre-monsoon) than their minimum (in the post-monsoon season). The high spatiotemporal resolution of PlanetScope imagery (~daily, 3 meter) shows that this cycle is driven by the appearance and expansion of small lakes in the upper debris-covered regions of these glaciers throughout the winter. Decadal-scale expansion of large, near-terminus lakes was identified on four of the glaciers (Khumbu, Lhotse, Nuptse, and Ambulapcha), while the remaining four showed no significant increases over the study period. The ~~annual~~seasonal variation in SGL area is of comparable or greater magnitude as decadal-scale changes, highlighting the importance of accounting for this seasonality when interpreting long-term records of SGL changes from sparse observations. The complex spatiotemporal patterns revealed in our analysis are not captured in existing regional-scale glacial lake databases, suggesting that more targeted efforts are needed to capture the true variability of SGLs on large scales.

## 1 Introduction

The processes controlling the response of debris-covered glaciers (DCGs) to changing climatic conditions are distinct from those of clean-ice glaciers and tend to be less well studied and understood (Brun et al., 2019; Miles et al., 2020). Supraglacial lakes (SGLs) on DCGs can increase ablation rates through increased radiation absorption, ice cliff calving, and efficient transfer of heat to the englacial and subglacial environments (Miles et al., 2022). Further, rapid drainage of these lakes ~~present~~presents a potential hazard to downstream communities and infrastructure (Miles et al., 2018; Rounce et al., 2017), particularly in cases where smaller ponds coalesce into large terminal lakes capable of causing catastrophic glacier lake outburst floods (Watanabe et al., 2009).

Understanding the evolution of SGLs on DCGs has been limited by difficulties associated with directly observing these  
25 features (Racoviteanu et al., 2022). The rugged topography of DCGs generally limits the scope of in situ investigations to  
single lakes and/or individual glaciers. Remote-sensing approaches to studying the glacier-wide spatial and temporal patterns  
in lake evolution have been limited by 1) the spatial resolution of freely available satellite imagery (e.g., Landsat and Sentinel-  
2) being large relative to the size of many SGLs, and 2) the infrequent revisit period of satellites acquiring higher spatial  
resolution imagery preventing detailed assessment of the rapid temporal evolution of these lakes.

30 Previous studies have found that SGLs tend to form in areas with low surface gradients and low glacier flow velocities  
(Reynolds, 2000). The temporal stability of individual lakes can vary widely, with some appearing stable on decadal scales,  
while others fill and drain annually, semi-annually, or seemingly randomly (Narama et al., 2017; Steiner et al., 2019). Seasonal-  
to-annual patterns in lake development have been observed, with links to ice velocity variations, water availability from precip-  
itation and snow/ice melt, and the opening or collapsing of englacial conduits (Benn et al., 2001; Mertes et al., 2017; Watson  
35 et al., 2018b).

There are few existing studies which have investigated the seasonal variations in SGL lake area on DCGs on a glacier-wide  
~~sealescales~~. These studies have generally relied on coarser-resolution Landsat imagery aggregated over decadal time periods  
(Miles et al., 2017; Narama et al., 2017), or have used a sensor integration approach with both optical and ~~synthetic aperture~~  
~~radar~~ Synthetic Aperture Radar (SAR) datasets (Wendleder et al., 2021). Further, the majority of these studies (including ours)  
40 have focused on DCGs in High Mountain Asia, and particularly in regions of the Himalaya and Karakoram which are impacted  
by the Indian summer monsoon.

These studies find that SGLs generally form in the early spring from the accumulation of rain and meltwater, grow in size  
through the pre-monsoon season (1 March–15 June), and then drain during the monsoon season (15 June–30 September). The  
frequent snow cover and frozen surfaces tend to make lake identification difficult during the winter, but SGLs are generally  
45 assumed to be stable or very slowly drain throughout the post-monsoon (1 October–30 November) and winter (1 December–28  
February) months (Watson et al., 2018b; Miles et al., 2017).

Despite these patterns in SGL area and drainage that have been observed over seasonal timescales, the majority of studies  
investigating SGL development on decadal timescales have not explicitly accounted for seasonality in lake area (e.g., Mohanty  
and Maiti, 2021; Watson et al., 2016; Steiner et al., 2019). Rather, these studies tend to utilize a series of individual higher-  
50 resolution images that cover a wide range of years but are captured at irregular seasonal timing.

The Improving our understanding of the dynamics of short-term SGL variability would allow us to differentiate between the  
confounding effects of seasonal and long-term trends in SGL area. Therefore, the goal of this study is to develop consistent  
observations of SGL evolution over daily-to-decadal timescales ~~. To do so, we integrate on eight glaciers in the Khumbu region~~  
of Nepal through the integration of PlanetScope satellite imagery (Planet Team 2017), Sentinel-2 and Landsat 5–9 imagery, and  
55 ~~in-situ field observations to investigate SGL dynamics on eight glaciers in the Khumbu region of Nepal~~ in situ field observations.

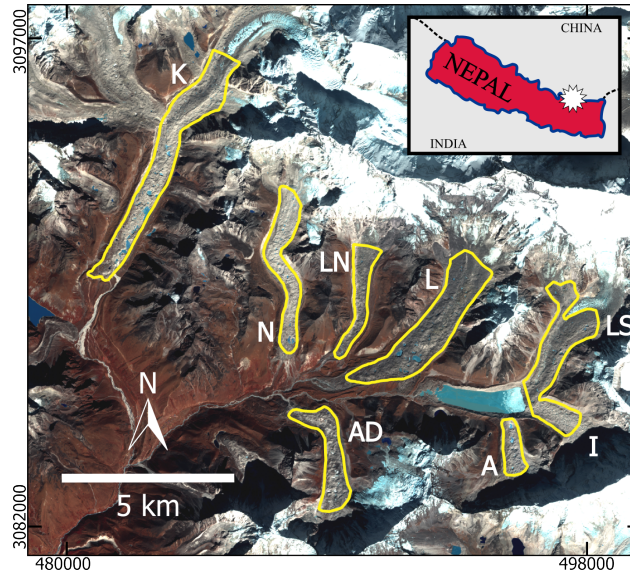


**Figure 1.** Sentinel-2 satellite image (13 November 2020) of the study area. The debris-covered areas of the eight glaciers are outlined in yellow. Letters adjacent to each glacier are shortened names (K=Khumbu, N=Nuptse, LN=Lhotse Nup, L=Lhotse, LS=Lhotse Shar, I=Imja, A=Ambulapcha, AD=Ama Dablam). Inset map shows the region's location within Nepal (indicated by the white star). [The coordinate frame indicates the Easting/Northing range of the figure within UTM Zone 45N.](#)

## 2 Study Area

We investigate SGL dynamics on eight glaciers in the Khumbu region of Nepal (Figure 1; Table S1). The glaciers in this region are characterized by ablation zones which have nearly continuous debris cover, slow ice flow velocities (<10 m/yr), and low-gradient surface slopes (<5°). Debris-covered areas range in elevation from 4800–5300 m, with debris-thickness tending to increase towards the glacier termini (Rounce et al., 2021). Five of the glaciers in this study have a southerly aspect and flow direction, two (Ambulapcha and Ama Dablam) flow north, and one (Imja) flows predominantly westward (Figure 1). Lhotse Shar and Imja flow into the rapidly-expanding Imja Tsho, resulting in increased ice flow velocities compared to the other glaciers in this study (Watanabe et al., 2009).

The climate in the Khumbu region is characterized by monsoonal summer seasons, during which the majority of [the 587 ± 34 mm of](#) annual precipitation falls, and cold and dry winter seasons (Perry et al., 2020). The limited winter precipitation leads to non-continuous snow cover on the study glaciers' surfaces throughout the winter, however cold air temperatures regularly resulted in frozen lake surfaces, particularly in the February–April time period.

### 3 Methods

In this study, we investigated the patterns of SGL development on time scales ranging from subseasonal to decadal. We achieved  
70 this by integrating multiple satellite remote sensing imagery sources. Each ~~individual source allows allows source provides~~  
unique observations, while together they build upon each other to inform us on their relative strengths and limitations. Our  
methodology is broadly broken into a two-step process built around identifying SGLs in PlanetScope, Landsat, and Sentinel-2  
imagery. We first developed a ~~novel robust~~ approach to delineating SGLs in high temporal resolution time series of PlanetScope  
75 imagery. From this dataset, we investigated the seasonal patterns in SGL variations over the 2017–2022 time period. We  
then used these high spatial resolution observations (3 m ~~scalespatial resolution~~) as a validation dataset to optimize SGL  
identification in coarser-resolution Landsat and Sentinel-2 imagery, allowing us to investigate the decadal-scale trends in SGL  
evolution at coarser spatial scale (10 m and 30 m). Direct field observations and ~~Unmanned Uncrewed~~ Aerial System (UAS)  
surveys from May 2023 provided additional insight into the ~~variable spatial and temporal patterns of SGL development which~~  
~~are found in the study area~~local-scale topography of these glaciers.

80 The use of ~~high-resolution high-resolution~~ PlanetScope imagery allowed us to identify supraglacial streams and very small  
lakes which may be more appropriately referred to as “ponds”. There is no clear consensus in previous literature on the  
differentiation between terming a supraglacial feature a “lake” versus a “pond”, and without in situ observations it is difficult  
to differentiate between a supraglacial “stream” which is flowing and stagnant ponded water. Therefore, in this paper we use  
the term “supraglacial lake” (SGL) to refer to any supraglacial hydrologic feature which we identify from satellite imagery.

85 The area of investigation (AOI) was limited to the debris-covered tongue of each glacier. These outlines were created by  
manually adjusting the glacier extents from the Randolph Glacier Inventory Version 6.0 (RGI Consortium 2017) to better match  
glacier margins in high-resolution satellite imagery in Google Earth Pro (sourced from Maxar imagery). Areas of exposed  
glacier ice were also manually excluded as they were frequently mis-classified as water. For this analysis, we separated Lhotse  
Shar and Imja into two glaciers, although they are classified as a single glacier in the Randolph Glacier Inventory Version 6.0.  
90 The outlines used for these two glaciers excluded the rapidly expanding terminal lake Imja Tsho for the entire time period, as  
the focus of this study was solely on SGLs.

~~Workflow diagram for delineating supraglacial lakes in PlanetScope imagery. The boxed items indicate intermediate products  
in the workflow, while unboxed, italicized labels indicate processing steps which are referred to in the text.~~

#### 3.1 SGL identification: Planet

95 We developed a ~~largely-automated semi-automated~~ workflow to identify lakes on DCGs in PlanetScope images (Figure 2).  
~~We applied this workflow over eight DCGs in the Khumbu region of Nepal over the S1). Images of the study area from the~~  
October 2017 to April 2022 time period (Table S1, Figure 1). ~~We identify lakes with ice or snow-covered surfaces in addition  
to unfrozen lakes by taking advantage of the high temporal resolution of the imagery (see Section 3.1.2).~~

##### 3.1.1 Data access and cleanup



100 Imagery covering the AOI was were searched for and downloaded using the Planet Orders API (Planet Team 2017). For each glacier, we selected images that (1) captured the entire glacier extent, (2) had less than 15% cloud cover across the entire image, and (3) contained four-band (RGB and near-infrared (NIR)), ortho-rectified, surface-reflectance data (the “ortho\_analytic\_4b\_sr” asset type). We additionally included pairs of images which were taken by the same satellite on the same day that, when combined, captured the entire glacier surface and each met criteria (2) and (3). A full list of all images meeting these criteria  
105 was compiled for the eight study glaciers. The ‘harmonize’ tool was used when ordering these images using the Planet Orders API. This tool brings the spectral response of each image in line with coincident Sentinel-2 imagery, ensuring a consistent spectral response across the multitude of individual sensors.

This entire image collection was downloaded to a local computer for additional processing and lake identification. For each glacier, images were merged together (if needed) and then clipped to the AOI extent. Each image was then manually inspected  
110 to ensure suitable data quality. Images with considerable cloud cover or snow cover, anomalous spectral responses, or poor band coregistration were discarded. This was the only manual intervention in the otherwise fully automated workflow.

Areas of cloud cover and terrain shadows were identified in each image and excluded from future analysis. Cloud-covered areas were classified using the Planet-provided usable data mask. We developed an approach to identify terrain shadows within PlanetScope images as dark, spatially-continuous areas. Further details on the shadow masking can be found in the  
115 supplementary material See the supplementary material for additional information on these steps.

### 3.1.1 Initial lake identification

SGLs were identified by separately classifying water and frozen lakes, and then applying a pixel-wise temporal smoothing algorithm to ensure a consistent evolution of the glacier surface. An initial classification of water (Figure 2bS1b) was performed by using a spatially-varying threshold on the normalized-difference water ratio (NDWI, green minus) (Gao, 1996), calculated  
120 using the reflectances in the green and near-infrared (NIR) divided by green plus NIR; (Gao, 1996)), which was calculated after applying scaling factors to convert band values to surface reflectance. bands as:

$$\frac{\text{Green} - \text{NIR}}{\text{Green} + \text{NIR}} \quad (1)$$

Each pixel was then classified as water if its NDWI was at least 0.10 greater than the mean NDWI of surrounding pixels within 150 meters (not including off-glacier areas, cloud cover, and terrain shadows) and with a minimum NDWI threshold of  
125 -0.15 (these thresholds were empirically determined). A final shadow masking step was also applied at this point, with pixels with average surface reflectance across visible (RGB) bands less than 0.02 excluded from being classified as water.

An initial classification of frozen lake surfaces (Figure 2bS1b) was performed using a similar spatially-varying threshold on the NIR band. Each pixel was classified as frozen water (ice) if the NIR digital number was at least 1000 greater than the mean NIR of surrounding pixels within 150 meters (not including off-glacier areas, cloud cover, and terrain shadows). In simple  
130 terms: areas of relatively high NDWI were initially classified as water, while areas of relatively high brightness in the NIR band were initially classified as lake ice. This initial ice classification does not differentiate between lake ice, glacier ice, and snow, however we take precautions to avoid including glacier ice and snow in the final products (described in Section 3.1.3).

The study extent was delineated to purposefully exclude areas of the glaciers that were not completely debris-covered, reducing the possibility of glacier ice being mis-classified as lake ice. Images with widespread snow cover were excluded (Section 3.1.1).  
135 Additionally, in later steps we only allow areas which were recently classified as water to be classified as frozen lakes (Section 3.1.3), limiting the effects of mistakenly identifying snow drifts or exposed ice cliffs as SGLs.

An ice flow correction was applied to each initial water and lake ice classification image to align them to a common date of 1 January 2020 (Figure 2eS1c). This removes the effects of lake advection due to ice flow and allows multi-year tracking of individual lakes. Glacier flow velocities were taken from 1985–2022 composite ITS\_LIVE velocity mosaics (Gardner et al.,  
140 2023) resampled to PlanetScope resolution.

### 3.1.1 Filtering and Smoothing

~~Following the initial classification of SGLs there was significant variability and noise in the time series due to variable image quality, occasional snow and cloud cover, and inconsistent spectral response across images. In order to reduce this noise and to~~  
Following initial lake identification, a series of filtering and smoothing approaches were applied to ensure a consistent temporal  
145 evolution of SGLs in our products ~~, we applied a series of filtering and smoothing steps (Figure 2d).~~

~~A pixel-wise temporal smoothing algorithm was applied to the initial water classification images to prevent individual pixels from rapidly switching between being classified as water and non-water. For each pixel, we collated the time series of all observations across the four year period. Individual observations were assigned a value of 1 if the pixel was identified as water and 0 if it was not. A Gaussian filter was then applied to this time series, using a Gaussian kernel with a standard deviation of~~  
150 ~~14 days. For each point, if the resulting smoothed value was greater than or equal to 50% of the potential maximum value (the value it would be if all observations were initially classified as water) then that pixel in that image was given a “smoothed” classification of water. All other observations were classified as non-water. The products at the end of this smoothing process (Figure 2d, Temporally Smoothed Water) represent the spatiotemporal distribution of unfrozen SGLs.~~

~~The temporally smoothed water products were then used to further constrain the classification of frozen lake surfaces (Figure~~  
155 ~~2d, Spatiotemporal Ice Masking). Each pixel which was initially classified as lake ice remained as a lake ice pixel only if it was also classified as water at any point within the preceding or following 60 days (resulting in the Filtered Ice product). This limited the mis-classification of snow drifts and ice cliffs as SGLs.~~

~~Finally, the filtered ice dataset was combined with the temporally smoothed water dataset, and the same Gaussian temporal smoothing was applied to this combined dataset, resulting in the final lake extent dataset. This provides the extent of all lakes,~~  
160 ~~including frozen and unfrozen, within each image and reduce noise caused by variable image quality, occasional snow and cloud cover, and inconsistent spectral response. See the supplementary material for additional information on these steps.~~

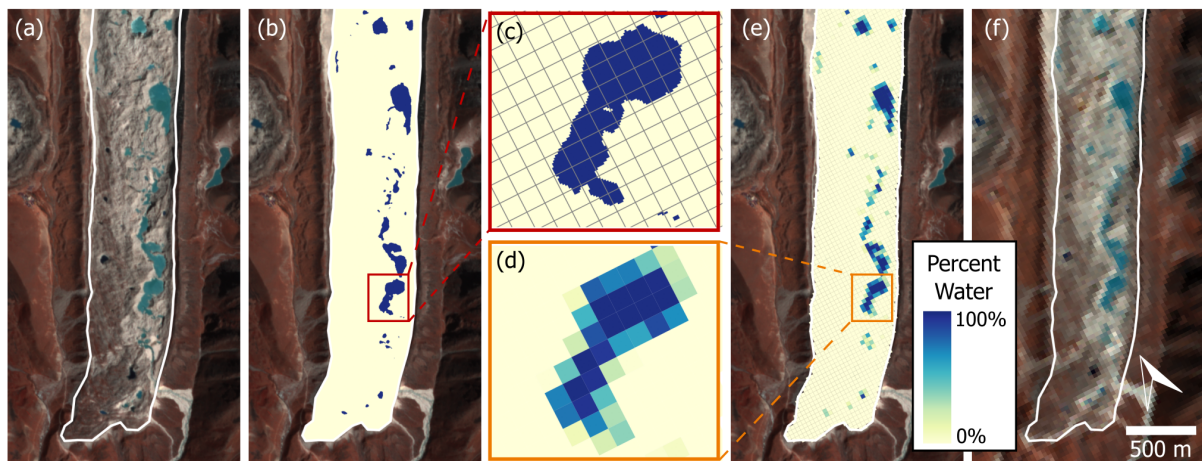


**Figure 2.** An example of the process of creating a Landsat-scale training dataset from Planet-derived lake extents. (a) shows an example PlanetScope image of the terminus of Khumbu Glacier on 24 October 2018, with the glacier extent outlined in black. (b) shows the lake extents in blue, from the automated PlanetScope workflow. (c) shows the Landsat pixel grid overlaid on the lake extents, for a subset of the glacier area. (d) shows the same area, resampled to Landsat pixel size and grid, colored by the percent of water cover within each pixel. (e) shows the full terminus area, resampled to the Landsat grid, colored by percent water coverage. (f) is a Landsat image from the same date (24 October 2018)

## 3.2 SGL identification: Landsat and Sentinel-2

### 3.2.1 Data access and cleanup

The Planet-derived SGL products were used as a training dataset for developing an optimized SGL identification approach for Landsat and Sentinel-2 imagery in our study area. All Landsat 5, 7, 8, 9 and Sentinel-2 [surface reflectance](#) imagery, spanning 165 the years 1988–2022, was downloaded from Google Earth Engine (n=1230 per glacier). ~~We used Landsat Tier 1 (Collection 2) surface reflectance products and Level-2A harmonized surface reflectance Sentinel-2 images.~~ The same debris-covered AOIs were used for all images to facilitate a direct comparison between all satellite sources and across the entire 35-year time frame. Each image of each glacier was manually checked, and images with significant cloud cover, snow cover, or shadows 170 over the majority of the glacier were discarded, resulting in an average of 940 images remaining for each glacier (Table S2). Shadowed areas in each image were masked using the Google Earth Engine `ee.Terrain.hillShadow()` function applied to the NASADEM (NASA JPL 2020) with image-specific sun azimuth and elevation as input. Additional remaining shadows were removed by thresholding on surface reflectance values in the green band (using [empirically-determined](#) values of 0.08 for Landsat images and 0.11 for Sentinel-2). Persistent exposed glacier ice, which was frequently present in older Landsat imagery 175 and mis-identified as water, was masked as described in the supplementary material.

### 3.2.1 Validation dataset creation

All Landsat 7, Landsat 8, and Sentinel-2 images with coincident Planet-derived lake extents were identified to be used as a training dataset. We defined suitable images as those which had at least three Planet-derived observations within the nine-day period centered on the Landsat/Sentinel-2 image date. For each of these training images, we resampled the corresponding Planet-derived lake extents to give a 30 m (Landsat) or 10 m (Sentinel-2) resolution product that indicated the percent water cover within each Sentinel-2/Landsat pixel (Figure 32). For lake identification in Landsat and Sentinel-2 imagery, we focused on only unfrozen lakes, rather than also attempting to identify frozen lake surfaces as we did in PlanetScope imagery. ~~The reason for this was that the limited temporal resolution of Landsat and Sentinel-2 did not allow for the same frozen water identification approach to be employed.~~ Thus, the Planet-derived products ~~we used for developing~~ used for the training dataset include only the lakes identified without employing the frozen lake identification (i.e., we used the temporally smoothed water product in Figure 2d S1d).

### 3.2.2 NDWI optimization and lake identification

Using the Planet-derived training dataset, we identified the optimal NDWI threshold (calculated after scaling images to surface reflectance) to use for binary classification of SGLs in Landsat and Sentinel-2 imagery (Watson et al., 2018a). For each sensor (Landsat 7, Landsat 8, and Sentinel-2) a single NDWI threshold was identified that minimized the difference between Planet-derived and Landsat/Sentinel-derived total lake area across the entire training dataset. There were no Landsat 5 images in the training dataset because the Landsat 5 mission ended in 2012. Landsat 9 images were included in our analysis, but there were insufficient images overlapping the PlanetScope validation dataset to reliably constrain an optimized NDWI threshold. Thus, the same NDWI threshold for Landsat 7 was used for Landsat 5 images, and the same threshold for Landsat 8 and 9, because the sensor band wavelength ranges are identical.

These optimized NDWI thresholds (Table 1) were then used to identify SGLs on the glacier surfaces across all available imagery, after removing shadowed areas and exposed glacier ice ([Section 3.2.1](#)). No additional smoothing was applied to these products, due to the limited temporal resolution compared to PlanetScope imagery.

### 3.3 Field observations

A field campaign was undertaken in May 2023 to collect ~~in-situ~~ in situ and drone-based observations of the study area. Perspective drone flights were flown on five glaciers (Lhotse Shar, Imja, Ambulapcha, Lhotse, and Lhotse Nup) to capture high resolution videos and photos of the debris-covered surfaces using a DJI Mavic 2 Pro and DJI Mavic Air 2s. Additionally, grid surveys were flown near the termini of Ambulapcha, Lhotse Nup, and Khumbu glaciers to create high-resolution Structure from Motion Multi-View Stereo (SfM) digital elevation models (DEMs) and orthomosaics. Grid surveys were flown ~60–90 meters above ground level, with nadir camera positioning and at least 70% overlap between images. SfM processing was completed in Agisoft Metashape. Ground control points (GCPs) were placed and surveyed for all three grid surveys, however there were no nearby operational base stations to use for ~~PPK processing~~ post-processing of these points, so they were not used in model

**Table 1.** The optimized NDWI threshold that was found for each Landsat and Sentinel-2 sensor.

Satellite	Optimized NDWI
Landsat 5 & 7	<del>0.172</del> <u>0.137</u>
Landsat 8 & 9	<del>0.226</del> <u>0.188</u>
Sentinel-2	<del>0.260</del> <u>0.250</u>

creation. Thus, model generation was based on UAV GPS locations. The model creation resulted in DEMs with 0.08 m ~~spatial scale~~ pixel spacing and orthomosaics with 0.04 m ~~spatial scale~~ pixel spacing.

## 210 4 Validation

A validation set for the Planet-derived lake extents was created by manually delineating SGLs in a total of 28 PlanetScope images of Lhotse, Nuptse, and Ambulapcha glaciers (Figure ~~S1~~S3). For each glacier, a series of cloud-free images spanning a range of approximately one year were selected, in order to capture the full annual cycle of SGL expansion and drainage. We used a  $\pm 1$  pixel (3 m) buffer for error estimation of these manual delineations (Gardelle et al., 2011). Further, the total SGL  
215 area on seven glaciers which were manually mapped by Watson et al. (2016) was compared to our results from concurrent months. While there is no overlap in the years investigated between our study and theirs (the latest imagery used in Watson et al. (2016) was from 2015), it provides a valuable constraint on the expected magnitude of SGL area.

## 5 Results

### 5.1 Lake delineation accuracy

#### 220 5.1.1 Planet

The Planet-derived SGL extents resulted in physically realistic, accurate delineations of SGLs at high spatiotemporal resolution (Figure 4, ~~Figure 53~~, Figure 4). The mean absolute error in total SGL area was 0.039 km<sup>2</sup> for Lhotse Glacier, 0.018 km<sup>2</sup> for Nuptse Glacier, and 0.004 km<sup>2</sup> for Ambulapcha Glacier. These are equal to errors of 0.75%, 0.66% and 0.41% of the total debris-covered area (from our AOIs) of each glacier respectively (25%, 33%, and 13% of the total lake-covered area).  
225 During the months with highest temporal density of suitable imagery (September–February), these errors are significantly lower (0.19%, 0.36%, and 0.28% of debris-covered area ~~,~~ and 7.6%, 19.1%, and 8.3% of the lake-covered area, respectively). ~~Further,~~ A direct comparison between our products and those from Watson et al. (2016), who derived SGL areas on these glaciers from high resolution imagery over the 2000-2015 time period) is not possible, because there is no overlap in the observational years. However, our automated SGL areas from similar annual timing showed good agreement with ~~results from~~

**Table 2.** Observations of lake count and area on individual glaciers. Note that the number of lakes on a glacier at a single point in time (i.e. Max. #) may be greater than the total number of lakes identified on the glacier over the entire time period (Lake #) if individual lakes merge together to create a single, larger lake. Minimum and maximum lake area and count for each glacier are provided in the supplementary material.

Glacier	Lake #	Lake area (m <sup>2</sup> )	Permanent lake # (%)	Min. #	Max. #	Min. area (m <sup>2</sup> )	Max. area (m <sup>2</sup> )
Ama Dablam	121	115974	3 (2.48%)	10	112	7641	57555
Ambulapcha	48	61749	0 (0%)	3	64	9081	55755
Imja	62	17964	0 (0%)	0	31	0	6498
Khumbu	619	571734	14 (2.26%)	88	690	162414	436536
Lhotse	589	423054	8 (1.36%)	51	442	54405	276912
Lhotse Nup	123	64800	1 (0.81%)	2	97	3465	34578
Lhotse Shar	368	197910	4 (1.09%)	27	318	22626	171522
Nuptse	201	116073	6 (2.99%)	22	138	32526	84213

230 ~~Watson et al. (2016) at similar annual timing (Figure S1) theirs (Figure S3), with the majority of their results falling within our~~  
inter-annual range of values ~~. A notable difference can be observed in the lake area on Khumbu Glacier, where our results show~~  
~~a greater SGL area than observed by Watson et al. (2016) which is likely due to the well-documented long-term expansion and~~  
~~coalescence of lakes near the terminus (Naito et al., 2000). Similarly, the large (average difference of 17.3% when discounting~~  
~~Imja and Lhotse Shar). The differences on Imja Glacier and Lhotse Shar Glacier (where we found smaller lake areas compared~~  
235 ~~to Watson et al. (2016)) may be attributed to changes in subglacial hydrology as the proglacial lake Imja Tsho expands (Bolch~~  
~~et al., 2008).~~

### 5.1.2 Landsat and Sentinel-2

The optimized NDWI thresholds for lake identification were found to be ~~0.172-0.137~~ for Landsat 5 and 7, ~~0.226-0.188~~ for  
Landsat 8 and 9, and ~~0.260-0.250~~ for Sentinel-2 images (Figure 6, Table 1); ~~with total errors across the entire validation dataset~~  
240 ~~being less than 1%, Figure S2). The optimized value for Sentinel-2 is similar to the value found by Watson et al. (2018a) of~~  
0.22. The optimized value they found for Landsat 8 is not directly comparable to our results because they used the modified  
NDWI (Xu, 2006) which uses a short wave infrared band in place of the near infrared band when calculating NDWI.

The ~~average median~~ per-image glacier-wide error in SGL area, compared to the coincident Planet-derived lake area, was  
~~0.4937%~~ for Landsat and ~~0.4334%~~ for Sentinel-2 (presented as a percentage of ~~total debris-covered Planet-derived lake~~  
245 ~~area), with values for individual glaciers ranging from 0.12%–0.99%, and 0.07%–1.04%–19% (Lhotse) to 100% (Imja), and 13%~~  
~~(Ambulapcha) to 60% (Imja) respectively (Table S3).~~



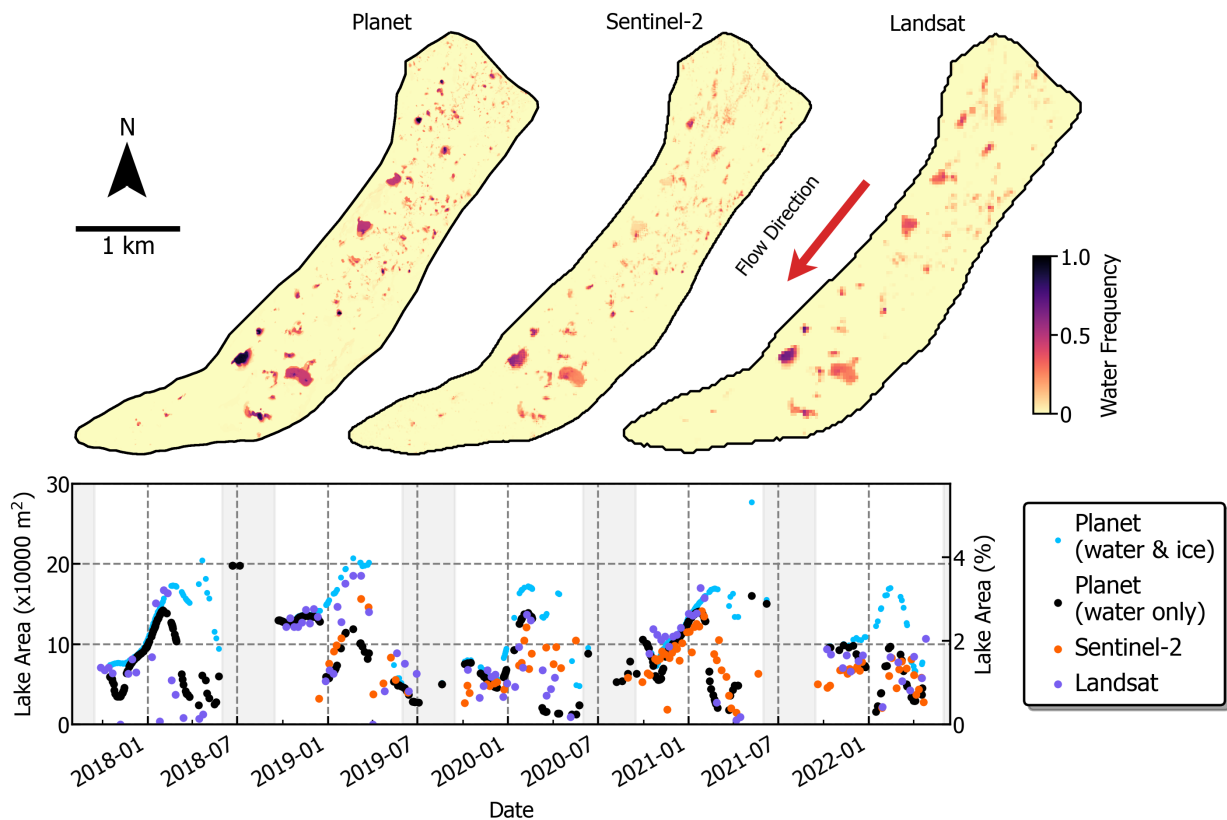


**Figure 3.** A comparison between the SGL extents and frequency in Planet, Sentinel-2 and Landsat imagery on Lhotse Glacier. The colorscale corresponds to the frequency each pixel was classified as water, with darker colors being more frequent. Only Landsat images from the 2018–2022 time period were used, to provide a more direct comparison with Planet and Sentinel-2. The time series plot shows the trend in total lake area for each sensor. Each point represents water identified in a single image. Planet-derived lake areas are shown for both the full methodology which includes frozen lake area (cyan) and the area if frozen lake area is excluded (black).

## 5.2 Short term dynamics

### 5.2.1 Seasonality in glacier-wide lake area

A pronounced seasonal cycle in total SGL area was found in the Planet-derived lake datasets (Figure 7, Figure S15, Figure S3). On most glaciers, the maximum glacier-wide SGL area (both frozen and open water) occurred in March (during the pre-monsoon season), decreased throughout the monsoon with a minimum area occurring in September, and then increased steadily throughout the post-monsoon and winter months (October–February) (Figure 75). For each glacier, the annual maximum SGL area is approximately twice the annual minimum (Table S4-S8), highlighting the magnitude of short-term variability these features can exhibit. While this cycle is most clearly seen in the high temporal resolution Planet-derived dataset, it is also

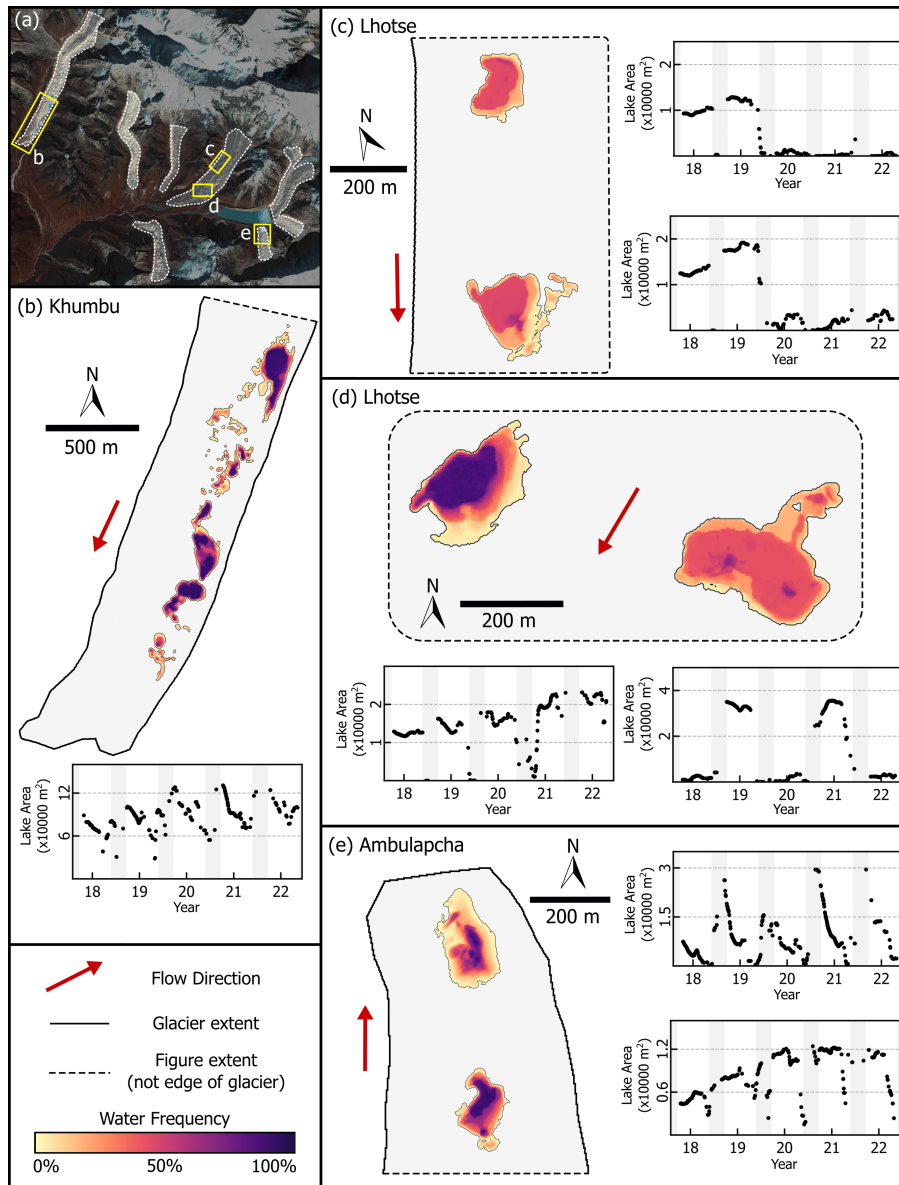


**Figure 4.** Water frequency maps and time series of select individual lakes or groups of lakes. Locations of each (b-e) are indicated in the top-left overview map. Lake maps are colored by water frequency (darker colors indicating more frequent water). The time series show the total area in individual Planet images. Grey shaded areas indicate monsoon season (15 June-30 September). Year tick-marks indicate the start of each year. Red arrows indicate the glacier flow direction.

255 apparent in Sentinel-2 and Landsat-derived time series, although frequent lake surface freezing in winter months (which was not classified in Landsat/Sentinel-2) obscures this trend in many years (Figure 43).

The winter-time increase in SGL area is not caused by an increase in the frozen SGL area (Figure [S2S4](#)). We find that the maximum frozen lake surface extent occurs in April, and minimal lake surface freezing occurs in the September–December time period during which unfrozen lake area is steadily increasing (Figure [S2S4](#)).

260 A detailed investigation of the five-year Planet-derived SGL inventory shows that the seasonal cycle in total SGL area (both frozen and unfrozen) is driven by the regular appearance and expansion of small lakes and supraglacial streams throughout the post-monsoon and winter months in the upper debris-covered regions further from the glacier termini (Figure [106](#), [Figure S5](#), [Figure S6](#)), rather than seasonal growth/shrinking of the larger lakes in the study region.

Between October and February in each of the five years on Lhotse Glacier, lake area increase was greater in regions further  
265 from ~~than the~~ terminus (Figure [10a6a](#)). Similarly, the total number of lakes increases throughout these months each year, with this driven predominantly by the increasing number of small lakes (lakes between 45 and 450 m<sup>2</sup>, or less than half of a single Landsat pixel) (Figure [10e6c](#)). Lastly, the relative contribution of smaller lakes to the total lake area increases between October and February each year (Figure [10b6b](#)). For example, lakes which are smaller in size than a single Landsat pixel (900 m<sup>2</sup>) account for an average of 18% of total lake area on Lhotse Glacier in October, but account for 34% of total lake area on  
270 average in February (Figure [10e](#)).

~~Taken together, these observations show that the increase in lake area between October and February is predominantly due to the appearance and expansion of small lakes and/or streams, rather than changes in area of larger lakes. This same pattern is~~  
[6b](#). ~~These same patterns are~~ observed (to varying degrees) on most glaciers in our study area, particularly on the four glaciers with the greatest lake area (Khumbu, Nuptse, Lhotse, and Lhotse Shar) (Figure [7](#), [Figures S36](#), [Figures S7–S10S14](#)).

## 275 5.2.2 Individual lake [seasonality dynamics](#)

The high spatial and temporal resolution of PlanetScope imagery allows investigation of the pattern of individual lake filling and drainage events (Figure [54](#)). Analysis of the pattern of individual lake dynamics reveals a complex system, where individual lakes may exhibit seasonal-to-multiannual patterns of surface area variations that greatly differ from the glacier-wide trends and even nearby lakes. ~~We found that larger lakes near glacier termini tend to be more temporally stable than smaller lakes~~  
280 ~~further from the terminus (Figure S11). Many of these larger lakes fill to their annual maximum extent at the end of the monsoon season and gradually decrease throughout the post monsoon and winter months (e. g. Figure 5b).~~

~~In our~~ ~~A total of 2131 unique lakes greater than or equal to 45 m<sup>2</sup> in area were identified in the Planet-derived dataset, we identified multiple large lakes~~ lake inventory across the five-year period, ranging in number from 48 to 619 across the eight glaciers (Table 2), with a total area of 1.57 km<sup>2</sup>. Of these lakes, only 36 were permanent (never completely draining across the  
285 entire study period), representing 1.69% of the lakes by count and 23.9% by area (at their maximum extents). These permanent lakes tend to be closer to the terminus of their respective glaciers, with an average normalized-distance of 0.47 (>47% of the distance from terminus to the upper debris-covered area) compared to 0.66 for all other lakes.

~~The recurrence frequency of the ephemeral (non-permanent) lakes varied substantially based on their size, with larger lakes re-appearing more frequently. Lakes smaller than a single Landsat pixel (900 m<sup>2</sup>) appeared on average in 2.0 years out of the 5~~  
290 ~~years of Planet observations, while lakes larger than this threshold appeared in 4.5 years on average (calculated by separating~~

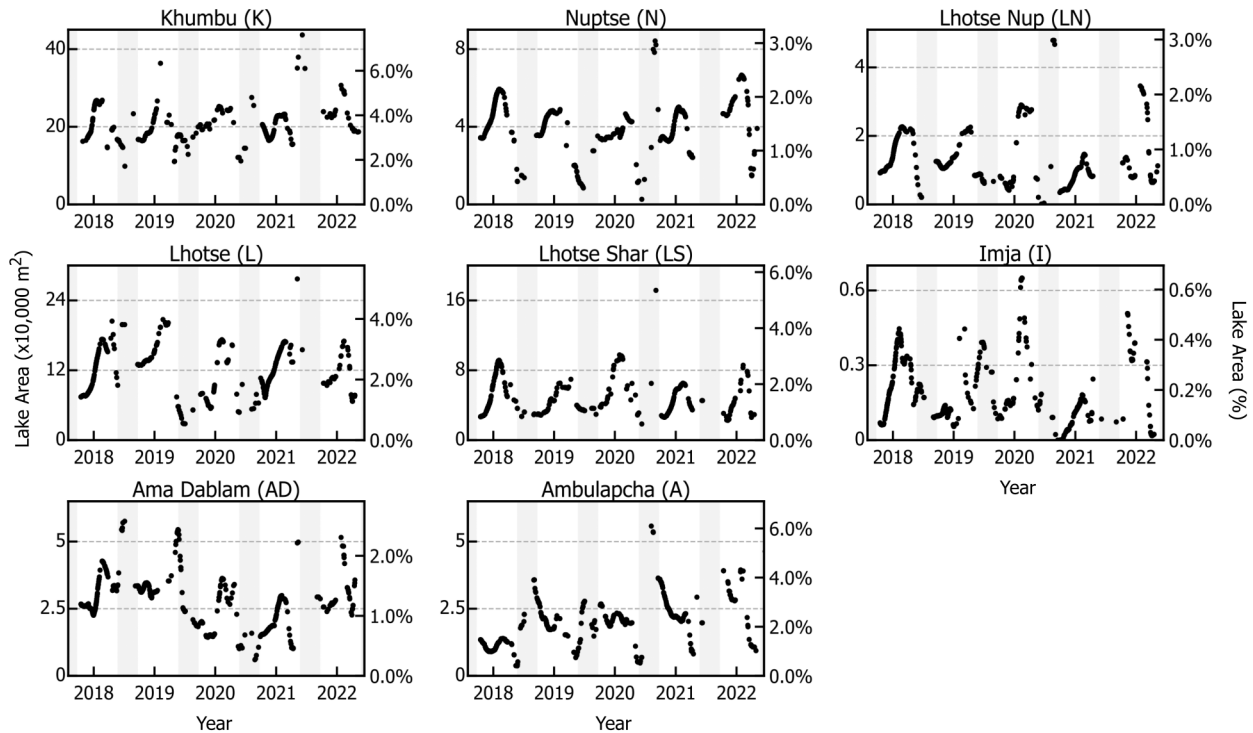


**Figure 5.** Time series of total SGL area on each glacier from PlanetScope imagery. Each point indicates the total lake area identified from the automated methodology. Grey shaded areas indicate the monsoon season (15 June–30 September). Left axis of each plot shows lake area, while right axis shows the values scaled to a percent of the total debris-covered area.

years on September 1). Only 355 (16.7%) of all lakes appeared in all five years, and the average size of these lakes was 3034 m<sup>2</sup>, compared to an average size of 277 m<sup>2</sup> for all others.

In some instances (on Khumbu and Ambulapcha glaciers) the number of lakes identified at a single point in time was greater than the total number of lakes identified on the glacier across the entire study period (Table 2). This may happen if unconnected lakes expand and eventually coalesce into a single lake, resulting in a greater lake area but smaller number of lakes.

We identified multiple lakes greater than 10000 m<sup>2</sup> which experienced rapid drainage events (Figure 5e.g. Figure 4), which all occur near the onset of the monsoon (May–June). Drainage events similar to these have been previously documented in this region and can cause significant impacts and damage to downstream communities and infrastructure (Rounce et al., 2017; Miles et al., 2018). In fact, the lake which we observed to rapidly drain twice (in 2019 and 2021) was also noted to be involved in the 2015 flood event documented by Rounce et al. (2017). Further analysis of the Landsat archive reveals six additional instances of this lake filling and draining within the 2008–2016 time period (and none prior to 2008), and the lake area increased each time that it refilled.

305 The total SGL area on Ambulapcha Glacier is dominated by two large lakes near the terminus that have distinct and contrasting seasonal patterns (Figure 4). The lake nearest to the terminus rapidly fills during the monsoon season each year and slowly drains throughout the post-monsoon, winter, and pre-monsoon seasons (Figure 4). In contrast, the second lake further from the terminus was consistently present over the duration of the PlanetScope observations, expanded throughout the five-year period, and completely drained during the onset of the monsoon in 2022 (Figure 4).

310 These lakes were empty during the May 2023 field campaign, allowing detailed topographic mapping of the lake basins (Figure S15). Both lakes appeared to have drained englacially, as evidenced by the presence of small ponds and exposed ice at the bottom of each basin. We used UAV-derived DEMs of the basins to construct an area-volume scaling relationship for each, by calculating the total surface area and volume with incrementally increasing water depths (0.2 m increments) to a maximum depth of 40 and 24 meters (for the lower and upper lake, respectively). The volume of the pre-existing ponded areas in each basin were estimated according to the relationship presented by Watson et al. (2018b), which built on the findings of Cook and Quincey (2015). The results from our artificial filling of the two basins found that the area-volume relationships of

315 each fall within the range of existing SGL observations (Watson et al., 2018b) (Figure S15).

### 5.3 Long-term trends

Complex patterns and trends in SGL evolution over decadal timescales are revealed by the Landsat-derived products, with notable differences being observed between different glaciers, between different parts of individual glaciers, and through time.

Over the 1988–2022 period, ~~three-two~~ of the eight glaciers (Khumbu, ~~Lhotse~~, and Ambulapcha) showed a statistically significant ( $P < 0.05$ ) positive trend in glacier-wide SGL area in Landsat-derived observations, based on a linear regression of the average annual lake area (Figure 8, ~~Figure S11, Table S3~~). ~~One glacier (Lhotse),~~ Two glaciers (Imja and Lhotse Shar) showed a statistically significant negative trend, while the remaining four did not have a statistically significant trend. Limiting the time period to only 2013–2022 (after the launch of Landsat 8), we find that only Khumbu has a statistically significant positive trend in SGL area, while ~~all-the~~ seven other glaciers have no statistically significant trend (Figure 8, ~~Figure S12, Figure S16~~).

325 ~~S12, Figure S16~~.

If we limit the area of investigation of each glacier to include only the lower half of the debris-covered area, where lake area shows less seasonal variation, then we find similar temporal trends. Three glaciers (Khumbu, Nuptse, and Ambulapcha) show an increasing trend over the 1988–2022 period, ~~one (Imja) shows two (Imja and Lhotse Shar) show~~ a decreasing trend, and the remaining ~~four-three~~ show no significant trend. In the more recent (2013–2022) period, three glaciers show a statistically significant increasing trend (Khumbu, Lhotse, and Ambulapcha), one (Ama Dablam) shows a decreasing trend (Figure 8, ~~Figure S12, Table S37, Figure S16, Table S9~~). The remaining show no statistically significant trend over the 2013–22 period, although increasing lake area on Nuptse ~~has increased while lake area on Lhotse Shar has decreased~~ is significant at the  $P < 0.1$  level.

330 ~~Figure 8, Figure S12, Table S37, Figure S16, Table S9~~.

Looking at the decadal-scale changes in spatial distribution of SGLs better illustrates the contrasting patterns among the ~~glaciers studied which we found in the time series trends~~ studied glaciers. The development and expansion of SGLs near the terminus of Khumbu Glacier is clearly visible, while at the same time there is a decrease in the frequency of lakes further

335 ~~glaciers studied which we found in the time series trends~~ studied glaciers.

up-glacier (Figure 98). Similarly complex patterns of SGL changes are apparent on all glaciers (Figures S13S17–S19S23), and offer complementary data to the time series investigation.

340 ~~Long term trends in SGL area on four glaciers as derived from Landsat imagery. Light grey dots show the lake area in individual Landsat images, while larger colored dots show the mean SGL area within each calendar year. (a-d) shows the SGL area over the entire glacier surface, while (e-h) show the lake area only on the near-terminus area (defined as the lower 50% of the glacier). Dotted and dashed lines show the linear regression of the annual averages for the entire time period (dotted) and only the 2013–2022 time period (dashed). Slopes and P-values are provided in Table S4.~~

## 6 Discussion

### 345 6.1 Comparison with previous SGL studies

The results of this study highlight how the high temporal resolution of PlanetScope imagery can be leveraged to advance our understanding of supraglacial lake dynamics. Prior analyses of the seasonal cycle of SGLs (Miles et al., 2017; Narama et al., 2017) have largely relied on coarser resolution Landsat imagery aggregated over decadal time periods in order to identify seasonal trends. While our results show a gradual increase in total lake areas throughout the winter leading up to the onset of  
350 the monsoon, these analyses (neither of which focus on the Khumbu region) have found that SGLs initially appear and fill in the pre-monsoon months (March to April) and then drain throughout the monsoon. A study by Wendleder et al. (2021) synthesized Sentinel-2, PlanetScope, and SAR datasets to construct a time series of SGL area over the summer months (April–September) on Baltoro Glacier (Pakistan). Similarly to the previous studies, Wendleder et al. (2021) also found that lakes appeared and expanded rapidly in the pre-monsoon spring months and drained throughout the monsoon summer.

355 The differences between these previous studies and our findings showing winter-time lake expansion may be due to methodological differences, such as coarser-resolution imagery being unable to capture smaller lakes which we observed with PlanetScope imagery, differences in regional climate causing different seasonal patterns of lake development, methodological differences (such as minimum lake size identifiable in Landsat images being 225 m<sup>2</sup> if the image is pansharpened), or not including frozen lakes in their inventories, and/or regional variations in SGL filling and draining. The debris-covered areas of the glaciers in  
360 our study region generally do not have continuous snow-cover for the entire winter, making SGL identification possible during these months. A study by Taylor et al. (2022) found wintertime (December to February) increases in SGL area on two of the three debris-covered glaciers they investigated on the Bhutan-Tibet border, and attributed this to variations in efficiency of supraglacial drainage systems between different glaciers and between seasons.

The seasonal variation in SGL area on individual glaciers that we find with our Planet-derived products is of higher magni-  
365 tude than decadal-scale trends in lake area change from the Landsat record. Many previous studies which use higher-resolution imagery to investigate SGLs on the same glaciers as this study have used a series of high-resolution images that may cover a wide range of years (up to multiple decades) but are captured at irregular seasonal timing (Mohanty and Maiti, 2021; Watson et al., 2016; Steiner et al., 2019). Our results suggest that without controlling for seasonality, such study designs are likely to



be insufficient for differentiating between the regular ~~seasonal-annual~~ cycle and long-term evolution of SGLs described here .  
370 ~~without controlling for seasonality (i.e. using only images captured during the same month across all years).~~

~~Watson et al. (2018b) presented in-situ~~ Watson et al. (2016) investigated the dynamics of SGLs on seven of the eight glaciers in our study (all but Ambulapcha) by using high-resolution (0.5–2 m) imagery over the 2000–2015 time period, with approximately 4 images of each glacier used. There was no direct overlap between their observations our PlanetScope-derived products (which are the closest in spatial resolution), but it provides an important opportunity to compare and validate the findings of each. The  
375 total area of SGLs identified on each glacier by Watson et al. (2016) was similar in magnitude to our results when comparing images from similar times of year (Figure S3). The limited image sample size in their study made it difficult to differentiate between the impacts of long-term SGL evolution and seasonal-to-annual SGL evolution, although they identified substantial inter- and intra-annual variability in SGL area. For glaciers other than Khumbu Glacier, the main findings were based on a series of three images from October 2011, December 2013, and January 2015. They found that total lake area increased on  
380 each glacier over this image series with the largest increases occurring in zones further from the terminus, and a trend towards smaller lakes accounting for a larger area (Watson et al., 2016, Figures 5 & 8). These results are identical to the annual pattern of wintertime lake development which we observed in our PlanetScope-derived dataset (Figure 6), providing validation of our findings while confirming that the trends observed by Watson et al. (2016) on these glaciers can likely be attributed to regular seasonal variations in SGL area rather than longer-term evolution of these glaciers.

385 ~~Watson et al. (2018b) presented in situ~~ observations on SGLs near the terminus of Khumbu glacier over the 2015–2016 year. They found that these lakes reached an annual maximum during the summer monsoon, followed by continuous ~~drainage throughout the winter months, which~~ shrinkage throughout the following post-monsoon and winter months. These results largely supported the findings ~~of by~~ Miles et al. (2017) and Narama et al. (2017) (~~which investigated SGLs in different basins within High Mountain Asia~~) of the of maximum SGL area occurring during the monsoon and shrinking in the post-monsoon  
390 and winter months. Our analysis showed a similar annual pattern of lake area in this ~~region same area~~ of Khumbu Glacier (Figure 5)4b), where the maximum lake area is observed at the end of the monsoon (September) each year, and the area decreases throughout the post-monsoon, winter, and pre-monsoon seasons. The discrepancy between the patterns seen in these lakes and ~~the pattern of~~ total glacier-wide SGL area ~~increasing throughout the post-monsoon and winter seasons (Figure 6)~~ shows that caution ~~should be applied is warranted~~ when extrapolating observations across the entire glacier, to other lakes, or  
395 to other glaciers, as individual lakes ~~and portions of the or portions of a~~ glacier often have unique spatiotemporal patterns

The limited availability of cloud-free imagery in the monsoon months limits our ability to draw conclusions about the specific timing and rate of drainage from our automated SGL identification approach. An approach focused on manual lake delineation during the monsoon and pre-monsoon time periods, or approaches using SAR data (Wendleder et al., 2021) would be more capable of answering these questions.

400 These findings highlight how, while satellite remote sensing platforms are capable of tracking changes in SGL area, they are not able to identify the specific processes which cause lakes to fill and drain. Detailed ~~in-situ in situ~~ observations such as those by Watson et al. (2018b) are needed to complement remotely-sensed observations.

The October-February seasonality of SGLs on Lhotse Glacier, with each row showing a unique year. (a) shows the percent of the glacier area with SGL coverage (y-axis) as a function of the normalized distance from the terminus (x-axis). Each line showing the area in a single month. (b) shows the cumulative SGL area (y-axis) with increasing lake size (x-axis), in each month. The x-axis ticks are shown in 900 m<sup>2</sup> increments (the size of a single Landsat pixel). Areas are normalized to a 0–1 scale to allow direct comparison between months and years. (c) shows the changes in the number of individual lakes within each image, binned into three different sizes. Blue are smaller in size than half of a Landsat pixel, orange are between one half and two Landsat pixels, and red are greater than two Landsat pixels.

## 6.2 Winter lake expansion

Our results showing an increase in total SGL area throughout the winter months is ~~seemingly counterintuitive~~ counter-intuitive, as the cold temperatures, limited precipitation, and minimal snow and ice melt would seemingly limit the availability of liquid water and suppress lake formation (E. S. Miles et al. 2017). ~~(Miles et al., 2017).~~ We hypothesize that ~~increased~~ absorption of solar radiation and conduction to underlying ice in areas with thin debris cover (Rounce et al., 2021; Miles et al., 2022) may lead to melt water production during winter months, while inefficient drainage systems result in this water pooling at the surface (Miles et al., 2020). This hypothesis is supported by the observation that wintertime lake appearance and expansion is most prominent in the upper debris covered regions of the glaciers (Figure 6), where debris cover is ~~likely thinnest~~ (Figure 10) thinnest, rather than at lower regions where thicker debris cover provides an insulating effect (Rounce et al., 2021). The inconsistent snow cover on the debris-covered tongues of these glaciers (particularly during the early winter months) would increase the potential solar radiation reaching their surface, particularly on the glaciers with more southerly aspects which also show the most consistent wintertime lake expansion (Figure ~~7~~ 5). This phenomenon may not be observed on glaciers in other regions with more consistent wintertime snow cover, or in regions with climates that are not dominated by the summer monsoon.

## 6.3 Area-volume sealing

~~Ambulapeha Glacier does not show the same annual cycle in total SGL area as the other seven glaciers do, due to two large lakes near the terminus that have distinct (and contrasting) seasonal patterns (Figure 5). The lake nearest to the terminus rapidly fills during the monsoon season each year and slowly drains throughout the post-monsoon, winter, and pre-monsoon seasons (Figure 5). In contrast, the second lake further from the terminus was consistently present over the duration of the PlanetScope observations, expanded throughout the five-year period, and nearly completely drained during the onset of the monsoon in 2022 (Figure 5).~~

~~The field observations and drone surveys carried out in May 2023 found that these lakes were completely drained, allowing detailed topographic mapping of the lake basins. Both lakes seemed to have drained englacially, based on the presence of small ponds and exposed ice at the bottom of each basin. We used high resolution DEMs of the basins to construct an area-volume sealing relationship for each, by calculating the total surface area and volume with incrementally increasing water depths (0.2 m increments) to a maximum depth of 40 and 24 meters (for the lower and upper lake, respectively). The volume of~~

the pre-existing ponded areas in each basin were estimated according to the relationship presented by Watson et al. (2018b), which built on the findings of Cook and Quincey (2015). The results from our artificial filling of the two basins found that the area-volume relationships of each fall within the range of existing SGL observations (Watson et al., 2018b).

440 The area-volume scaling relationship for the two large lake basins on Ambulapcha Glacier (purple and orange lines). Black points show previous observations of SGL areas and volumes on Khumbu Glacier by Watson et al. (2018b), and the black dashed line is the best-fit relationship presented in the study. (a) shows the area-volume relationship (in log-log scale). (b) shows the percent error that results from using the best-fit equation for estimating volume from an observed area. Grey shaded area shows the 37% mean error from all observations in Watson et al. (2018b). (c) shows the UAS-derived DEM (hillshade with elevation overlaid) and approximate extents of the two lake basins.

### 445 6.3 Long-term trends

Our findings highlight many of the difficulties associated with monitoring the long-term evolution of SGLs. The seasonal variations in glacier-wide lake area are of similar or greater magnitude to the long-term changes (Figure 5, Figure 7, Figure 8S16). The long-term trends in lake area are variable depending on the time period and the specific area of the glacier investigated. We found that SGL area has increased near the terminus on four of the glaciers investigated (Khumbu, Lhotse, Ambulapcha, 450 and Nuptse) over the 2013–2022 time period (Figure 7, Table S9). This observed expansion and possible future coalescing of near-terminus lakes on these glaciers suggests that they should be closely monitored for future outburst flood risk (Benn et al., 2012).

An efficient supraglacial stream network on the surface of Lhotse Shar, combined with a highly incised notch in the terminal moraine, as observed from field observations, has likely prevented large lakes from persisting on its surface. In contrast, 455 Khumbu Glacier has a similarly efficient supraglacial stream network near its terminus, which also flows off the glacier through a deep notch in the terminal moraine, but has nevertheless developed many large SGLs that have been continuously expanding and coalescing in recent years (Naito et al., 2000). This contrasting behavior, compared to Lhotse Shar, may be due to a slightly lower surface gradient and greater number of ice cliffs on Khumbu Glacier. However, the presence of the outlet stream deeply incised into the moraine on Khumbu glacier Glacier may help to limit future SGL expansion.

460 The recent SGL expansion on Lhotse Glacier is unique due to the distance up-glacier at which this expansion is occurring (Figure 10, Figure S17) within this study region. The lower section of the glacier, downstream from the area of lake expansion, is relatively steep (up to 5° near the terminus), has a well established stream drainage network, and has little-to-no terminal moraine. The lake expansion has occurred predominantly in an area ~2 km from the terminus (Figure S22), at a point where the surface gradient lowers to 2° and maintains that slope for ~3 km up-glacier. The lack of a terminal moraine suggests that 465 the risk of a large terminal lake (similar to Imja Tsho) forming on Lhotse Glacier is low, however sudden drainage of the large SGLs englacially and through the existing supraglacial stream network remains possible (Rounce et al., 2017).

The Our long-term time series of SGLs on Imja and Lhotse Shar glaciers that we present here shows show only a portion of the lakes that are present throughout the time period because a static glacier outline was used. These glaciers were significantly larger in the late 1980s, and have been retreating rapidly due to the expansion of their proglacial lake (Imja Tsho). Their transi-

470 tion to lake-terminating glaciers has likely inhibited the growth of supraglacial lakes due to increasing surface velocities. The expansion of Imja Tsho is certain to have further significant effects and feedbacks on the subglacial, englacial, and supraglacial hydrologic systems of the glacier (Watanabe et al., 2009), but those are not ~~fully~~ investigated in this paper.

#### 6.4 Methodological limitations

The ~~automated~~-semi-automated approaches used for SGL delineation in Landsat, Sentinel, and PlanetScope imagery substantially increases the amount of data which can be efficiently analyzed relative to manual identification methods. However, it is important to understand the limitations of these automated methods in order to appropriately use the derived products.

The geolocation accuracy of PlanetScope imagery can be poor (up to 10 m RMSE at the 90th percentile) (Planet Team, 2022), particularly in complex and steep terrain such as the Himalayas. ~~This can result,~~ resulting in multi-pixel misalignment between images, ~~or even or~~ between individual bands within the same image. This can inhibit the ability to track spatial and temporal evolution of features as small as SGLs and introduce substantial noise into the data. Differences in the sensors on individual satellites can further add noise. Taking advantage of the high temporal resolution of PlanetScope imagery allows ~~you to remove the filtering out of~~ much of the noise and gain increased confidence in the results, ~~but,~~ However, significant cloud cover during the pre-monsoon and monsoon seasons, in addition to consistently frozen lake surfaces in the February-April months, lowers the confidence of the results during those times. ~~(Figure S3, Figure S4). The decrease in total SGL area that we see on many glaciers between March and June each year is likely due to these cloud and ice limitations, rather than a true decrease in lake area.~~

Higher geolocation accuracy of Landsat and Sentinel-2 imagery have better geolocation accuracy, and more consistency in their spectral responses than PlanetScope imagery, which allows them images was observed compared to PlanetScope images relative to their spatial resolution, both between images and between bands in single images. This accuracy, combined with a high degree of consistency in the spectral quality of images, allows Landsat and Sentinel-2 to overcome many of the ~~mentioned limitations~~ limitations inherent to using PlanetScope imagery. However, the lower spatial and temporal resolution (particularly for Landsat) means that smaller SGLs and short-term variations are difficult or impossible to identify. Additionally, identifying lakes with frozen surfaces is more difficult without the dense temporal resolution that was used for the Planet-derived dataset, further obscuring winter-time changes in lake area.

#### 6.5 Comparison with regional-scale databases

A comparison between the SGL extents produced in this study with regional- or global-scale glacier lake inventories (Chen et al., 2021; Wang et al., 2020; Racoviteanu et al., 2021; Shugar et al., 2020) suggests that existing datasets do not capture the full behavior of SGLs through space and time (Figure 129). We found that three time-varying inventories (Chen et al., 2021; Wang et al., 2020; Shugar et al., 2020) considerably underestimated the extent of modern SGLs on these eight glaciers. The Shugar et al. (2020) dataset, which used the full Landsat archive to map glacial lakes across the entire globe in five-year time intervals, does not include any SGLs on these glaciers due to the minimum size threshold of 50000 m<sup>2</sup> that was used, ~~and,~~ Additionally, two areas of glacial ice were misclassified as lakes in the 2020 product (not shown on Figure 129) because they

are up-glacier from the study region). ~~For the ten years of~~ [The Chen et al. \(2021\) Hi-MAG dataset provides annual glacial lake outlines in the](#) ~~Chen et al. (2021) Hi-MAG dataset, a~~ [High Mountain Asia region for the 2008–2017 time period derived from Landsat imagery and using a 8100 m<sup>2</sup> minimum size threshold. On these glaciers a single lake was identified on Lhotse Glacier in one year, seven total lakes on Khumbu Glacier across four years, and no lakes on the other glaciers in our study area. The Wang et al. \(2020\) dataset provides glacial lakes outlines in the High Mountain Asia region for two time steps \(1990 and 2018\) using manual delineation of Landsat imagery and a 5400 m<sup>2</sup> minimum size threshold. Their 2018 data found five SGLs on Lhotse Glacier, two on Ama Dablam Glacier, and five on Khumbu Glacier \(and no lakes on the others\).](#)

510 In contrast, Racoviteanu et al. (2021) ~~present a comparable~~ [used a spectral unmixing model on Landsat 8 imagery to identify supraglacial ponds on debris-covered glaciers in the Himalayas during the post-monsoon season \(September–November\) in 2015. Their spectral unmixing approach allowed for identification of ponds that were smaller than a single Landsat pixel. The derived dataset show a comparable magnitude \(falling within the range of our PlanetScope-derived products\) and spatial distribution of SGLs to our study findings, but only provides data for a single time step. In summary, the stark differences](#)

515 ~~between these prior studies and our findings highlight how recent advances in satellite remote sensing can be leveraged to improve regional- to global-scale glacial lake studies, particularly for SGLs on debris-covered glaciers, given their-~~

[While the differences in SGL number and area of these datasets \(Chen et al., 2021; Wang et al., 2020; Shugar et al., 2020\) relative to our findings is due primarily to the minimum size threshold used \(and the overall aims of their studies\), these comparisons highlight how our current understanding of SGL dynamics over regional or global scales is very limited. Studies](#)

520 [which focus primarily on the unique spatial and temporal characteristics of SGLs \(e.g. Racoviteanu et al., 2021\) are needed to better characterize these features.](#)

## 7 Conclusions

In this paper, we presented an automated approach to identifying SGLs on debris-covered glaciers from PlanetScope, Sentinel-2, and Landsat imagery. Lake identification in Landsat and Sentinel-2 was optimized using coincident Planet observations.

525 These methods were used to map lake extents on eight glaciers in the Khumbu region of Nepal over the 1988–2022 time period.

A regular annual cycle in SGL development was found, with the annual minimum in glacier-wide lake area occurring at the end of the monsoon season followed by a gradual increase throughout the winter season and a maximum in February and March, followed by drainage throughout the monsoon season (Figure 75). The magnitude of seasonal variations were

530 considerable, with the annual maximum being approximately double the annual minimum (Tables S4–S8). This annual cycle is driven by the appearance and gradual expansion of small lakes in the upper debris-covered regions of these glaciers throughout the winter months, while larger lakes near the glacier termini tended to be more stable or slowly drain during the winter. Over decadal timescales, near-terminus lakes were observed to be expanding and coalescing ~~over~~ on four of the glaciers (Khumbu, Lhotse, Ambulapcha, and Nuptse) (Figure 8, ~~Figure S127~~, [Figure S16](#)), highlighting the need for continued observation to

535 evaluate the evolving glacier lake outburst flood hazards they present.

The annual cycle ~~is-in~~ SGL area which we identified has important implications for interpreting prior observations of SGLs. The intra-annual timing of observations must be considered in order to differentiate long-term trends from seasonal variability. A comparison between our results and existing regional-scale glacier lake inventories showed that the complex spatiotemporal patterns are not fully captured in these datasets. Our findings highlight the unique capabilities of satellite remote sensing  
540 platforms to track changes in SGL area over time. However, detailed ~~in-situ-in situ~~ observations are needed to complement these remotely-sensed observations to better understand the processes controlling SGL evolution.

*Code and data availability.* PlanetScope imagery is available through Planet (<https://www.planet.com/>). Landsat imagery is available through the USGS EarthExplorer platform (<https://earthexplorer.usgs.gov/>). Sentinel-2 imagery is available through the Copernicus Open Access Hub (<https://scihub.copernicus.eu/>). Derived products (image-specific lake extents, DEMs, and orthomosaics) and analytical scripts are available  
545 via Zenodo (<https://doi.org/10.5281/zenodo.8173102>).

*Author contributions.* Concept and design were done by LZ, DM; programming by LZ; formal analyses by LZ; Fieldwork by LZ, DM, SWM, JJ; DEM generation by JJ, DM; writing by LZ; edit and review by LZ, DM, SWM, JJ; visualization by LZ; funding acquisition and project administration by DM, SWM;

*Competing interests.* The authors declare that they have no competing interests

550 *Acknowledgements.* This effort was supported by NASA's ~~High-mountain~~ High Mountain Asia research program (NNH15ZDA001N-HMA, award number 80NSSC20K1343). The authors thank Himalayan Research Expeditions for important logistical support during fieldwork. We thank Anna Wendleder and Duncan Quincey for their constructive reviews which improved the quality of the manuscript.



## References

- Benn, D., Bolch, T., Hands, K., Gulley, J., Luckman, A., Nicholson, L., Quincey, D., Thompson, S., Toumi, R., and Wiseman, S.: Response of debris-covered glaciers in the Mount Everest region to recent warming, and implications for outburst flood hazards, *Earth-Science Reviews*, 114, 156–174, <https://doi.org/10.1016/j.earscirev.2012.03.008>, 2012.
- Benn, D. I., Wiseman, S., and Hands, K. A.: Growth and drainage of supraglacial lakes on debris-mantled Ngozumpa Glacier, Khumbu Himal, Nepal, *Journal of Glaciology*, 47, 626–638, <https://doi.org/10.3189/172756501781831729>, 2001.
- Bolch, T., Buchroithner, M. F., Peters, J., Baessler, M., and Bajracharya, S.: Identification of glacier motion and potentially dangerous glacial lakes in the Mt. Everest region/Nepal using spaceborne imagery, *Natural Hazards and Earth System Sciences*, 8, 1329–1340, <https://doi.org/10.5194/nhess-8-1329-2008>, 2008.
- Brun, F., Wagnon, P., Berthier, E., Jomelli, V., Maharjan, S. B., Shrestha, F., and Kraaijenbrink, P. D. A.: Heterogeneous Influence of Glacier Morphology on the Mass Balance Variability in High Mountain Asia, *Journal of Geophysical Research: Earth Surface*, 124, 1331–1345, <https://doi.org/10.1029/2018JF004838>, 2019.
- Chen, F., Zhang, M., Guo, H., Allen, S., Kargel, J. S., Haritashya, U. K., and Watson, C. S.: Annual 30 m dataset for glacial lakes in High Mountain Asia from 2008 to 2017, *Earth System Science Data*, 13, 741–766, <https://doi.org/10.5194/essd-13-741-2021>, 2021.
- Cook, S. J. and Quincey, D. J.: Estimating the volume of Alpine glacial lakes, *Earth Surface Dynamics*, 3, 559–575, <https://doi.org/10.5194/esurf-3-559-2015>, 2015.
- Gao, B.-c.: NDWI—A normalized difference water index for remote sensing of vegetation liquid water from space, *Remote Sensing of Environment*, 58, 257–266, [https://doi.org/10.1016/S0034-4257\(96\)00067-3](https://doi.org/10.1016/S0034-4257(96)00067-3), 1996.
- Gardelle, J., Arnaud, Y., and Berthier, E.: Contrasted evolution of glacial lakes along the Hindu Kush Himalaya mountain range between 1990 and 2009, *Global and Planetary Change*, 75, 47–55, <https://doi.org/10.1016/j.gloplacha.2010.10.003>, 2011.
- Gardner, A., Fahnestock, M., and Scambos, T.: MEASURES ITS\_LIVE Regional Glacier and Ice Sheet Surface Velocities, Version 1, <https://doi.org/10.5067/6II6VW8LLWJ7>, 2023.
- Mertes, J. R., Thompson, S. S., Booth, A. D., Gulley, J. D., and Benn, D. I.: A conceptual model of supra-glacial lake formation on debris-covered glaciers based on GPR facies analysis: GPR Facies Analysis of Spillway Lake, Ngozumpa Glacier, Nepal, *Earth Surface Processes and Landforms*, 42, 903–914, <https://doi.org/10.1002/esp.4068>, 2017.
- Miles, E. S., Willis, I. C., Arnold, N. S., Steiner, J., and Pellicciotti, F.: Spatial, seasonal and interannual variability of supraglacial ponds in the Langtang Valley of Nepal, 1999–2013, *Journal of Glaciology*, 63, 88–105, <https://doi.org/10.1017/jog.2016.120>, 2017.
- Miles, E. S., Watson, C. S., Brun, F., Berthier, E., Esteves, M., Quincey, D. J., Miles, K. E., Hubbard, B., and Wagnon, P.: Glacial and geomorphic effects of a supraglacial lake drainage and outburst event, Everest region, Nepal Himalaya, *The Cryosphere*, 12, 3891–3905, <https://doi.org/10.5194/tc-12-3891-2018>, 2018.
- Miles, E. S., Steiner, J. F., Buri, P., Immerzeel, W. W., and Pellicciotti, F.: Controls on the relative melt rates of debris-covered glacier surfaces, *Environmental Research Letters*, 17, 064 004, <https://doi.org/10.1088/1748-9326/ac6966>, 2022.
- Miles, K. E., Hubbard, B., Irvine-Fynn, T. D., Miles, E. S., Quincey, D. J., and Rowan, A. V.: Hydrology of debris-covered glaciers in High Mountain Asia, *Earth-Science Reviews*, 207, 103 212, <https://doi.org/10.1016/j.earscirev.2020.103212>, 2020.
- Mohanty, L. K. and Maiti, S.: Regional morphodynamics of supraglacial lakes in the Everest Himalaya, *Science of The Total Environment*, 751, 141 586, <https://doi.org/10.1016/j.scitotenv.2020.141586>, 2021.

- Naito, N., Nakawo, M., Kadota, T., and Raymond, C. F.: Numerical simulation of recent shrinkage of Khumbu Glacier, Nepal Himalayas, p. 11, 2000.
- 590 Narama, C., Daiyrov, M., Tadono, T., Yamamoto, M., Kääh, A., Morita, R., and Ukita, J.: Seasonal drainage of supraglacial lakes on debris-covered glaciers in the Tien Shan Mountains, Central Asia, *Geomorphology*, 286, 133–142, <https://doi.org/10.1016/j.geomorph.2017.03.002>, 2017.
- Perry, L. B., Matthews, T., Guy, H., Koch, I., Khadka, A., Elmore, A. C., Shrestha, D., Tuladhar, S., Baidya, S. K., Maharjan, S., Wagnon, P., Aryal, D., Seimon, A., Gajurel, A., and Mayewski, P. A.: Precipitation Characteristics and Moisture Source Regions on Mt. Everest in the Khumbu, Nepal, *One Earth*, 3, 594–607, <https://doi.org/10.1016/j.oneear.2020.10.011>, 2020.
- 595 Planet Team: PLANETSCOPE PRODUCT SPECIFICATIONS, [https://assets.planet.com/docs/Planet\\_PSScene\\_Imagery\\_Product\\_Spec\\_letter\\_screen.pdf](https://assets.planet.com/docs/Planet_PSScene_Imagery_Product_Spec_letter_screen.pdf), 2022.
- Racoviteanu, A., Nicholson, L., Glasser, N., Miles, E., Harrison, S., and Reynolds, J.: Debris-covered glacier systems and associated glacial lake outburst flood hazards: challenges and prospects, *Journal of the Geological Society*, 179, jgs2021–084, <https://doi.org/10.1144/jgs2021-084>, 2022.
- 600 Racoviteanu, A. E., Nicholson, L., and Glasser, N. F.: Surface composition of debris-covered glaciers across the Himalaya using linear spectral unmixing of Landsat 8 OLI imagery, *The Cryosphere*, 15, 4557–4588, <https://doi.org/10.5194/tc-15-4557-2021>, 2021.
- Reynolds, J. M.: On the formation of supraglacial lakes on debris-covered glaciers, p. 9, 2000.
- 605 Rounce, D. R., Byers, A. C., Byers, E. A., and McKinney, D. C.: Brief communication: Observations of a glacier outburst flood from Lhotse Glacier, Everest area, Nepal, *The Cryosphere*, 11, 443–449, <https://doi.org/10.5194/tc-11-443-2017>, 2017.
- Rounce, D. R., Hock, R., McNabb, R. W., Millan, R., Sommer, C., Braun, M. H., Malz, P., Maussion, F., Mouginot, J., Seehaus, T. C., and Shean, D. E.: Distributed Global Debris Thickness Estimates Reveal Debris Significantly Impacts Glacier Mass Balance, *Geophysical Research Letters*, 48, <https://doi.org/10.1029/2020GL091311>, 2021.
- 610 Shugar, D. H., Burr, A., Haritashya, U. K., Kargel, J. S., Watson, C. S., Kennedy, M. C., Bevington, A. R., Betts, R. A., Harrison, S., and Strattman, K.: Rapid worldwide growth of glacial lakes since 1990, *Nature Climate Change*, 10, 939–945, <https://doi.org/10.1038/s41558-020-0855-4>, 2020.
- Steiner, J. F., Buri, P., Miles, E. S., Ragettli, S., and Pellicciotti, F.: Supraglacial ice cliffs and ponds on debris-covered glaciers: spatio-temporal distribution and characteristics, *Journal of Glaciology*, 65, 617–632, <https://doi.org/10.1017/jog.2019.40>, 2019.
- 615 Taylor, C. J., Carr, J. R., and Rounce, D. R.: Spatiotemporal supraglacial pond and ice cliff changes in the Bhutan–Tibet border region from 2016 to 2018, *Journal of Glaciology*, 68, 101–113, <https://doi.org/10.1017/jog.2021.76>, 2022.
- Wang, X., Guo, X., Yang, C., Liu, Q., Wei, J., Zhang, Y., Liu, S., Zhang, Y., Jiang, Z., and Tang, Z.: Glacial lake inventory of high-mountain Asia in 1990 and 2018 derived from Landsat images, *Earth System Science Data*, 12, 2169–2182, <https://doi.org/10.5194/essd-12-2169-2020>, 2020.
- 620 Watanabe, T., Lamsal, D., and Ives, J. D.: Evaluating the growth characteristics of a glacial lake and its degree of danger of outburst flooding: Imja Glacier, Khumbu Himal, Nepal, *Norsk Geografisk Tidsskrift - Norwegian Journal of Geography*, 63, 255–267, <https://doi.org/10.1080/00291950903368367>, 2009.
- Watson, C. S., Quincey, D. J., Carrivick, J. L., and Smith, M. W.: The dynamics of supraglacial ponds in the Everest region, central Himalaya, *Global and Planetary Change*, 142, 14–27, <https://doi.org/10.1016/j.gloplacha.2016.04.008>, 2016.
- 625 Watson, C. S., King, O., Miles, E. S., and Quincey, D. J.: Optimising NDWI supraglacial pond classification on Himalayan debris-covered glaciers, *Remote Sensing of Environment*, 217, 414–425, <https://doi.org/10.1016/j.rse.2018.08.020>, 2018a.

- Watson, C. S., Quincey, D. J., Carrivick, J. L., Smith, M. W., Rowan, A. V., and Richardson, R.: Heterogeneous water storage and thermal regime of supraglacial ponds on debris-covered glaciers: Water storage and thermal regime of supraglacial ponds, *Earth Surface Processes and Landforms*, 43, 229–241, <https://doi.org/10.1002/esp.4236>, 2018b.
- 630 Wendleder, A., Schmitt, A., Erbertseder, T., D'Angelo, P., Mayer, C., and Braun, M. H.: Seasonal Evolution of Supraglacial Lakes on Baltoro Glacier From 2016 to 2020, *Frontiers in Earth Science*, 9, 725 394, <https://doi.org/10.3389/feart.2021.725394>, 2021.
- Xu, H.: Modification of normalised difference water index (NDWI) to enhance open water features in remotely sensed imagery, *International Journal of Remote Sensing*, 27, 3025–3033, <https://doi.org/10.1080/01431160600589179>, 2006.

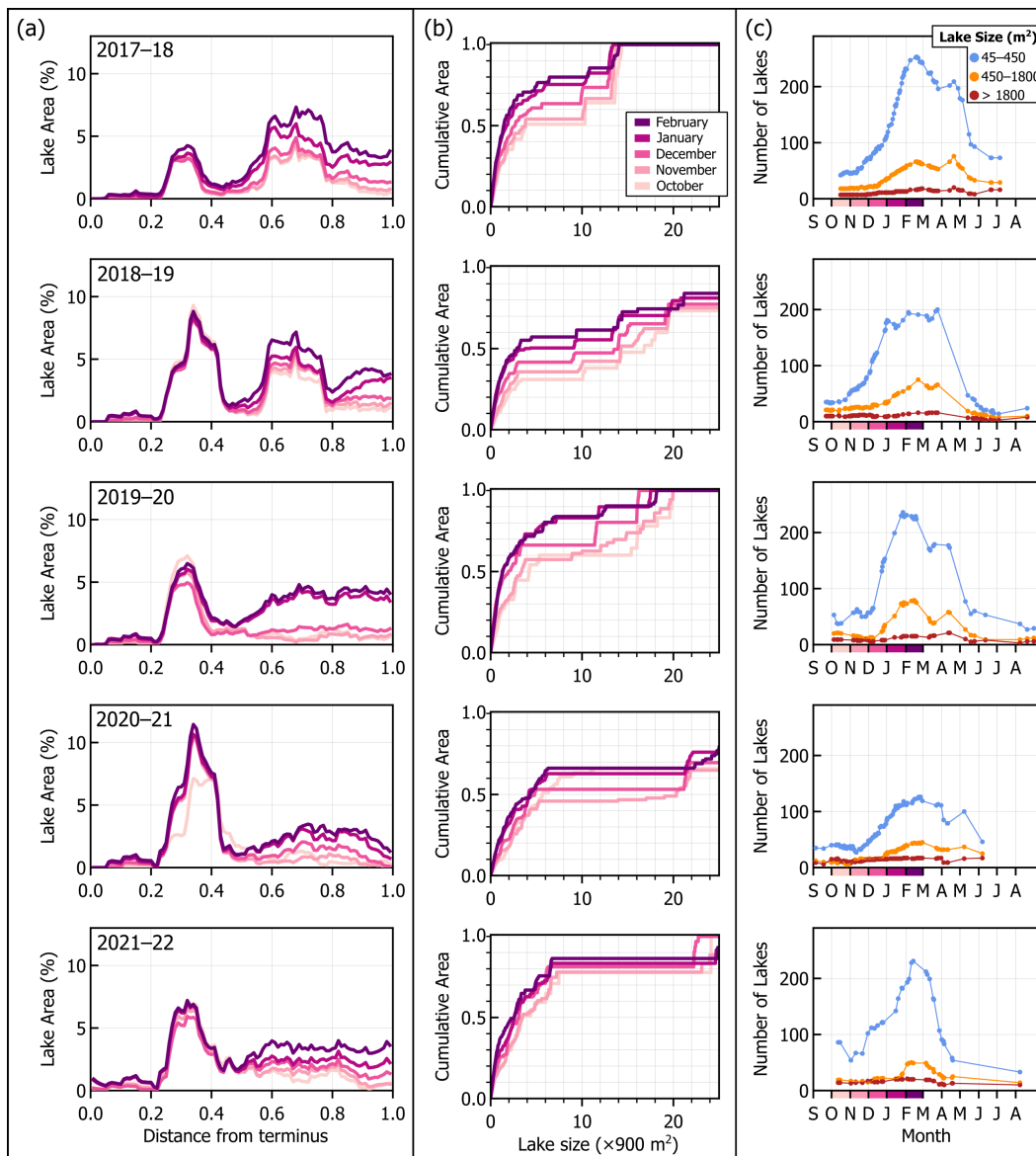


**Figure 6.** The October-February seasonality of SGLs on Lhotse Glacier, with each row showing a unique year. (a) NDWI-optimization results for each satellite. Each horizontal bar shows the range-percent of NDWI values for Landsat and Sentinel-2 pixels in the validation dataset-glacier area with the indicated percent-water-cover SGL coverage (aggregated-in-5%-bins y-axis). Dots indicate the mean, grey bars show the range-containing 90% as a function of all observations. Horizontal lines and the shown number indicate normalized distance from the optimized-NDWI-value for each sensor, which minimized the net-error over the validation-dataset-terminus (bx-axis) and (c) compare. Each line showing the SGL-area identified in PlanetScope imagery and in Landsat/Sentinel-2 coincident imagery using the optimized thresholds, with each point representing a single imagemonth. (b) shows these values as the total-lake-cumulative SGL area, while (ey-axis) scales them by the total-glacier-debris-covered-area. Mean-absolute-error-with-increasing-lake-size (MAE x-axis) is, in each month. The x-axis ticks are shown for Landsat-in 900 m<sup>2</sup> increments (purple the size of a single Landsat pixel). Areas are normalized to a 0-1 scale to allow direct comparison between months and Sentinel-2-years. (orange) results-on-shows the changes in the number of individual lakes within each plot image, binned into three different sizes. Blue are smaller in size than half of a Landsat pixel, orange are between one half and two Landsat pixels, and red are greater than two Landsat pixels.

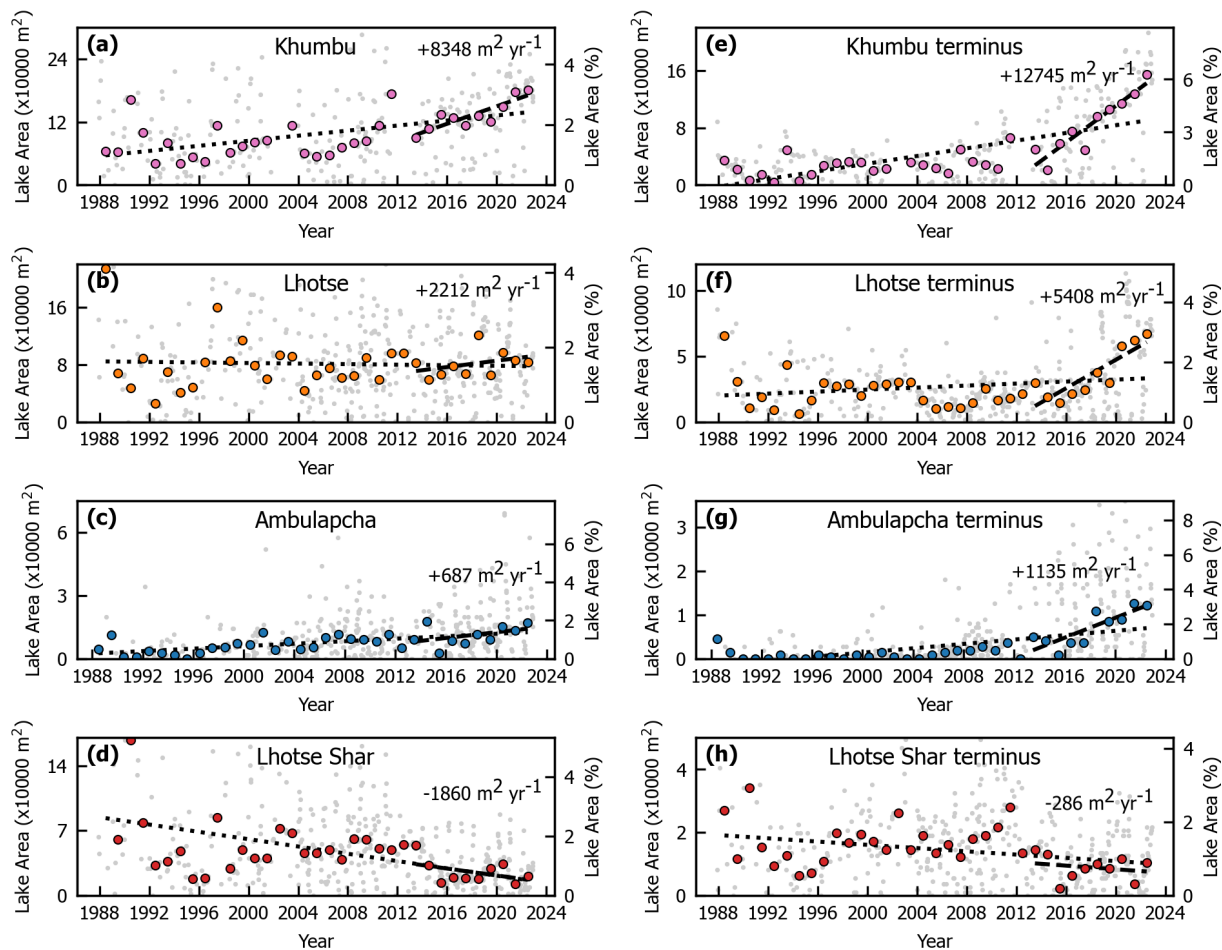


**Figure 7.** Time-series of total Long term trends in SGL area on each glacier four glaciers as derived from PlanetScope-Landsat imagery. Each-point indicates Light grey dots show the total-lake area identified from in individual Landsat images, while larger colored dots show the automated methodology. Grey shaded areas indicate monsoon season. Left axis of mean SGL area within each plot-calendar year. (a-d) shows lake-the SGL area over the entire glacier surface, while right-axis shows- (e-h) show the values scaled to a percent of lake area only on the total debris-covered near-terminus area (defined as the lower 50% of the glacier). Dotted and dashed lines show the linear regression of the annual averages for the entire time period (dotted) and only the 2013–2022 time period (dashed). Labeled slopes correspond to the 2013–2022 linear regression. All slopes and P-values are provided in Table S9.

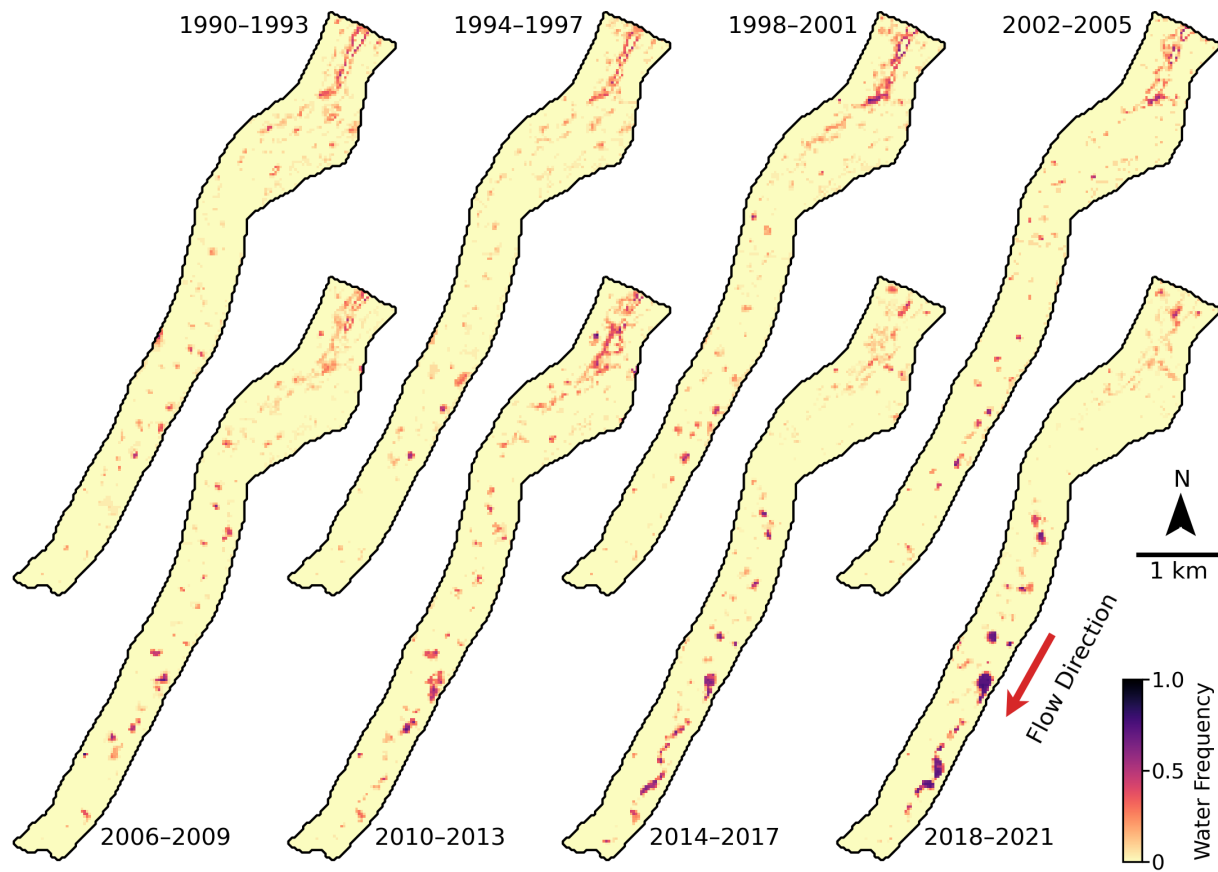


**Figure 8.** SGL frequency maps of Khumbu Glacier as derived from Landsat imagery. Each figure shows the water distribution aggregated within four-year intervals. Colors show the frequency with which each pixel was identified as water, with darker colors indicating more frequent water.



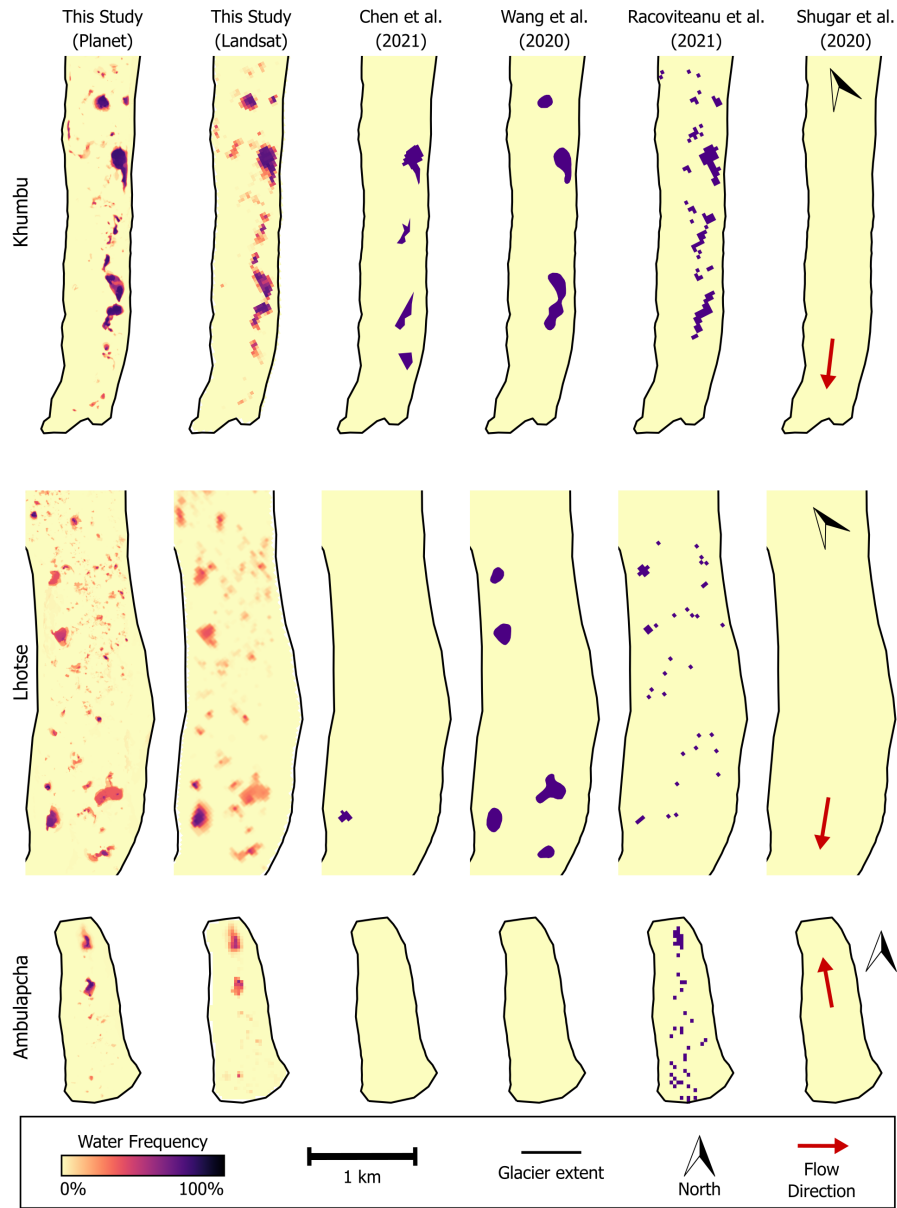


**Figure 9.** A comparison between our Planet-derived and Landsat-derived lake extents and publicly available regional-scale inventories (Chen et al., 2021; Wang et al., 2020; Racoviteanu et al., 2021; Shugar et al., 2020).

# SUPPLEMENTARY MATERIAL: Seasonal to decadal dynamics of supraglacial lakes on debris-covered glaciers in the Khumbu Region, Nepal

Lucas Zeller<sup>1</sup>, Daniel McGrath<sup>1</sup>, Scott W. McCoy<sup>2</sup>, and Jonathan Jacquet<sup>2</sup>

<sup>1</sup>Department of Geosciences, Colorado State University, Fort Collins, CO 80523, USA

<sup>2</sup>Department of Geological Sciences and Engineering, University of Nevada, Reno, NV 89557, USA

**Correspondence:** Lucas Zeller (Lucas.Zeller@colostate.edu)

## 1 ~~PlanetScope Shadow Masking~~ Planet: Data access and cleanup

Imagery covering the AOI was searched for and downloaded using the Planet Orders API (Planet Team 2017). For each glacier, we selected images that (1) captured the entire glacier extent, (2) had less than 15% cloud cover across the entire image, and (3) contained four-band (RGB and near-infrared (NIR)), ortho-rectified, surface-reflectance data (the “ortho\_analytic\_4b\_sr” asset type). We additionally included pairs of images which were taken by the same satellite on the same day that, when combined, captured the entire glacier surface and each met criteria (2) and (3). A full list of all images meeting these criteria was compiled for the eight study glaciers. The ‘harmonize’ tool was used when ordering these images using the Planet Orders API. This tool brings the spectral response of each image in line with coincident Sentinel-2 imagery, ensuring a consistent spectral response across the multitude of individual sensors.

This entire image collection was downloaded to a local computer for additional processing and lake identification. For each glacier, images were merged together (if needed) and then clipped to the AOI extent. Each image was then manually inspected to ensure suitable data quality. Images with considerable cloud cover or snow cover, anomalous spectral responses, or poor band coregistration were discarded.

Areas of cloud cover and terrain shadows were identified in each image and excluded from future analysis. Cloud-covered areas were classified using the Planet-provided usable data mask. We developed an approach to identify terrain shadows within PlanetScope images as dark, spatially-continuous areas (described in detail below).

## 2 Planet: Shadow Masking

A novel texture-based approach was developed to identify and mask out terrain shadowing in PlanetScope images. Shadows were identified on the glacier surface as large, continuous areas that were dark and had little spatial variation in brightness.

These areas were identified using a multi-step process. First, areas of very high confidence shadow (shadow “seeds”) were identified. These were identified if it met the following criteria:

1. The average surface brightness in visible bands was less than 1000 (using the image digital numbers).
2. At least 75% of on-glacier pixels within 99 meters had surface brightness less than 1000
3. The standard deviation of surface brightness of pixels within 99 meters was less than 50

25 These areas of shadow seeds were then iteratively expanded to include the continuous regions surrounding them with pixel brightness below the 1000 DN threshold in visible bands, with small voids and gaps filled.

### 3 Planet: Filtering and smoothing

30 A pixel-wise temporal smoothing algorithm was applied to the initial water classification images to prevent individual pixels from rapidly switching between being classified as water and non-water. For each pixel, we collated the time series of all observations across the 2017–2022 period. Individual observations were assigned a value of 1 if the pixel was identified as water and 0 if it was not. A Gaussian filter was then applied to this time series, using a Gaussian kernel with a standard deviation of 14 days. For each point, if the resulting smoothed value was greater than or equal to 50% of the potential maximum value (the value it would be if all observations were initially classified as water) then that pixel in that image was given a “smoothed” classification of water. All other observations were classified as non-water. The products at the end of this smoothing process

35 (Figure 2d, Temporally Smoothed Water) represent the spatiotemporal distribution of unfrozen SGLs.

The temporally smoothed water products were then used to further constrain the classification of frozen lake surfaces (Figure 2d, Spatiotemporal Ice Masking). Each pixel which was initially classified as lake ice remained as a lake ice pixel only if it was also classified as water at any point within the preceding or following 60 days (resulting in the Filtered Ice product). This limited the mis-classification of snow drifts and ice cliffs as SGLs. Finally, the filtered ice dataset was combined with the

40 temporally smoothed water dataset, and the same Gaussian temporal smoothing was applied to this combined dataset, resulting in the final lake extent dataset. This provides the extent of all lakes, including frozen and unfrozen, within each image.

### 4 **Landsat Glacier Ice Masking**

Continuously exposed areas of glacier ice in Landsat images were identified using thresholding on the normalized difference snow index (NDSI) and blue band surface reflectance. As a first step, areas of snow/ice were identified as pixels with an NDSI

45 value greater than 0.2 and blue reflectance greater than 0.35. In order to avoid mis-classifying temporary snow cover, ice cliffs, or frozen lake surfaces as glacier ice we then applied a temporal smoothing to these products. For each Landsat image, pixels were given a final classification of glacier ice if that pixel was identified as ice using the aforementioned thresholds in greater than 60% of all Landsat images captured within the surrounding four years (two years before and after). These final glacier ice extents were then excluded from being classified as water. A final filtering step was also applied to remove occasional linear

50 artifacts in Landsat 5 near-infrared bands. Pixels where the difference between the green and near infrared reflectance (green minus near-infrared) was greater than 0.2 were masked out and not included in the analysis.

**Table S1.** ~~Number of observations and physical~~ Physical characteristics of each of the eight glaciers investigated. Note that all columns, other than “Total Glacier Size” refer to only the areas of investigation (AOI) used in this study. Ice flow velocities are given by the mean plus/minus one standard deviation. Note that Imja and Lhotse Shar (\*) are considered a single glacier in RGI 6.0 (RGI Consortium, 2017). Debris thicknesses were taken from Rounce et al. (2021), and flow velocities were taken from NASA ITS\_LIVE velocity mosaics (Gardner et al., 2022)

Glacier	Debris-covered Area (km <sup>2</sup> , within AOI)	Total Glacier Size (km <sup>2</sup> , RGI 6.0)	Glacier Length (km, within AOI)	Average debris thickness (m, within AOI)	Flow velocity (m yr <sup>-1</sup> , within AOI)
Ama Dablam	2.23	4.82	3.87	1.04	0.76 ±0.96
Ambulapcha	0.91	1.92	1.72	0.51	0.82 ±0.40
Imja	1.01	14.27*	1.59	0.20	1.38 ±1.39
Khumbu	5.74	19.10	8.09	0.82	1.53 ±2.97
Lhotse	5.21	6.83	5.81	0.13	3.30 ±6.06
Lhotse Nup	1.60	2.84	3.54	0.44	1.02 ±1.25
Lhotse Shar	3.21	14.27*	3.41	0.43	3.35 ±4.40
Nuptse	2.77	3.69	5.20	0.33	3.05 ±4.07

**Table S2.** Number of images for each glacier from each source, after manual filtering of images with cloud cover, snow cover, or poor image quality.

Glacier	Planet	Landsat 5	Landsat 7	Landsat 8	Landsat 9	Sentinel-2
Pre-filtering		324	394	204	20	288
Ama Dablam	495	148	174	91	6	83
Ambulapcha	467	139	169	98	10	95
Imja	411	167	190	113	12	111
Khumbu	306	174	0	104	9	108
Lhotse	371	153	181	89	10	101
Lhotse Nup	468	162	209	97	12	112
Lhotse Shar	338	160	183	96	13	116
Nuptse	422	160	173	92	9	115

**Table S3.** Error statistics for Landsat and Sentinel-2 SGL identification on each glacier. Comparing Planet-derived lake area to Landsat Sentinel-2 derived area. Presented as the mean-median per-image difference in SGL area across all coincident-validation imagery for each glacier (MAE, in m<sup>2</sup>), and then normalized by debris-covered-area-image-specific SGL (as %). Bias is computed by subtracting Landsat/Sentinel-2 derived SGL area from PlanetScope-derived area.

Glacier	Landsat 7 & 8		Sentinel-2	
	MAE (m <sup>2</sup> and %)	Bias (m <sup>2</sup> and %)	MAE (m <sup>2</sup> and %)	Bias (m <sup>2</sup> and %)
Ama Dablam	<del>6231</del> <u>(0.2794752)</u> (49.7%)	<del>3557</del> <u>(0.158207)</u> (-1.3%)	<del>5181</del> <u>(0.2322915)</u> (26.3%)	<del>1520</del> <u>(0.068648)</u> (4.1%)
Ambulapcha	<del>4213</del> <u>(0.4581994)</u> (21.2%)	<del>3969</del> <u>(0.431572)</u> (-4.3%)	<del>3906</del> <u>(0.4272505)</u> (13.0%)	<del>3377</del> <u>(0.3691996)</u> (-11.4%)
Imja	<del>1212</del> <u>(0.120940)</u> (100.0%)	<del>988</del> <u>(0.098828)</u> (-61.7%)	<del>705</del> <u>(0.070264)</u> (59.9%)	<del>589</del> <u>(0.059233)</u> (-23.2%)
Khumbu	<del>56465</del> <u>(0.98731797)</u> (19.8%)	<del>52140</del> <u>(0.91222950)</u> (-14.2%)	<del>59841</del> <u>(1.04348391)</u> (30.7%)	<del>59841</del> <u>(1.04348391)</u> (-30.1%)
Lhotse	<del>29923</del> <u>(0.57411475)</u> (19.2%)	<del>25956</del> <u>(0.4984149)</u> (+4.4%)	<del>38414</del> <u>(0.54617441)</u> (25.7%)	<del>12240</del> <u>(0.2365562)</u> (-6.1%)
Lhotse Nup	<del>6107</del> <u>(0.3813285)</u> (55.1%)	<del>6085</del> <u>(0.3803285)</u> (-36.8%)	<del>3549</del> <u>(0.2212223)</u> (38.1%)	<del>1646</del> <u>(0.1031371)</u> (-19.7%)
Lhotse Shar	<del>24582</del> <u>(0.76611016)</u> (36.8%)	<del>24582</del> <u>(0.76610809)</u> (-28.1%)	<del>19489</del> <u>(0.60814422)</u> (44.0%)	<del>17527</del> <u>(0.54612512)</u> (-31.5%)
Nuptse	<del>18310</del> <u>(0.66310143)</u> (35.6%)	<del>18068</del> <u>(0.65410143)</u> (-30.8%)	<del>12981</del> <u>(0.46911345)</u> (40.1%)	<del>12699</del> <u>(0.45911345)</u> (-40.7%)
Overall	<del>14542</del> <u>(0.4865436)</u> (36.8%)	<del>13322</del> <u>(0.4452079)</u> (-23.6%)	<del>14895</del> <u>(0.4265796)</u> (34.3%)	<del>12182</del> <u>(0.3362618)</u> (-21.6%)

**Table S4.** Lake number and area minimums (min.) and maximums (max.) for each glacier in 2018.

<u>Glacier</u>	<u>2018 min. (#)</u>	<u>2018 max. (#)</u>	<u>2018 min. (area)</u>	<u>2018 max (area)</u>
<u>Ama Dablam</u>	<u>18</u>	<u>72</u>	<u>22563</u>	<u>57555</u>
<u>Ambulapcha</u>	<u>4</u>	<u>35</u>	<u>9081</u>	<u>35658</u>
<u>Imja</u>	<u>4</u>	<u>23</u>	<u>612</u>	<u>4464</u>
<u>Khumbu</u>	<u>176</u>	<u>646</u>	<u>162414</u>	<u>268362</u>
<u>Lhotse</u>	<u>82</u>	<u>402</u>	<u>74124</u>	<u>204399</u>
<u>Lhotse Nup</u>	<u>17</u>	<u>65</u>	<u>9189</u>	<u>22626</u>
<u>Lhotse Shar</u>	<u>44</u>	<u>272</u>	<u>26739</u>	<u>91449</u>
<u>Nuptse</u>	<u>33</u>	<u>125</u>	<u>34047</u>	<u>59337</u>

**Table S5.** Lake number and area minimums (min.) and maximums (max.) for each glacier in 2019.

<u>Glacier</u>	<u>2019 min. (#)</u>	<u>2019 max. (#)</u>	<u>2019 min. (area)</u>	<u>2019 max (area)</u>
<u>Ama Dablam</u>	<u>31</u>	<u>85</u>	<u>29016</u>	<u>54441</u>
<u>Ambulapcha</u>	<u>6</u>	<u>42</u>	<u>17244</u>	<u>35739</u>
<u>Imja</u>	<u>3</u>	<u>18</u>	<u>549</u>	<u>4455</u>
<u>Khumbu</u>	<u>157</u>	<u>690</u>	<u>163863</u>	<u>363519</u>
<u>Lhotse</u>	<u>86</u>	<u>399</u>	<u>128691</u>	<u>207162</u>
<u>Lhotse Nup</u>	<u>18</u>	<u>67</u>	<u>10494</u>	<u>22554</u>
<u>Lhotse Shar</u>	<u>43</u>	<u>285</u>	<u>28710</u>	<u>69687</u>
<u>Nuptse</u>	<u>34</u>	<u>118</u>	<u>35406</u>	<u>48906</u>

**Table S6.** Lake number and area minimums (min.) and maximums (max.) for each glacier in 2020.

<u>Glacier</u>	<u>2020 min. (#)</u>	<u>2020 max. (#)</u>	<u>2020 min. (area)</u>	<u>2020 max (area)</u>
<u>Ama Dablam</u>	<u>30</u>	<u>92</u>	<u>14382</u>	<u>36279</u>
<u>Ambulapcha</u>	<u>12</u>	<u>64</u>	<u>17262</u>	<u>55755</u>
<u>Imja</u>	<u>1</u>	<u>31</u>	<u>855</u>	<u>6498</u>
<u>Khumbu</u>	<u>165</u>	<u>572</u>	<u>183492</u>	<u>275481</u>
<u>Lhotse</u>	<u>103</u>	<u>442</u>	<u>54405</u>	<u>172557</u>
<u>Lhotse Nup</u>	<u>14</u>	<u>97</u>	<u>4131</u>	<u>29007</u>
<u>Lhotse Shar</u>	<u>48</u>	<u>318</u>	<u>29547</u>	<u>97596</u>
<u>Nuptse</u>	<u>30</u>	<u>138</u>	<u>33264</u>	<u>84213</u>

**Table S7.** Lake number and area minimums (min.) and maximums (max.) for each glacier in 2021.

<u>Glacier</u>	<u>2021 min. (#)</u>	<u>2021 max. (#)</u>	<u>2021 min. (area)</u>	<u>2021 max (area)</u>
<u>Ama Dablam</u>	<u>10</u>	<u>73</u>	<u>7641</u>	<u>49788</u>
<u>Ambulapcha</u>	<u>9</u>	<u>33</u>	<u>20304</u>	<u>36405</u>
<u>Imja</u>	<u>0</u>	<u>18</u>	<u>0</u>	<u>2448</u>
<u>Khumbu</u>	<u>115</u>	<u>405</u>	<u>164619</u>	<u>436536</u>
<u>Lhotse</u>	<u>79</u>	<u>292</u>	<u>63693</u>	<u>276912</u>
<u>Lhotse Nup</u>	<u>9</u>	<u>54</u>	<u>3465</u>	<u>14625</u>
<u>Lhotse Shar</u>	<u>45</u>	<u>188</u>	<u>26190</u>	<u>171522</u>
<u>Nuptse</u>	<u>22</u>	<u>112</u>	<u>32526</u>	<u>82215</u>

**Table S8.** Lake number and area minimums (min.) and maximums (max.) for each glacier in 2022.

<u>Glacier</u>	<u>2022 min. (#)</u>	<u>2022 max. (#)</u>	<u>2022 min. (area)</u>	<u>2022 max (area)</u>
<u>Ama Dablam</u>	<u>40</u>	<u>112</u>	<u>23940</u>	<u>51534</u>
<u>Ambulapcha</u>	<u>18</u>	<u>44</u>	<u>27927</u>	<u>46323</u>
<u>Imja</u>	<u>3</u>	<u>26</u>	<u>729</u>	<u>5076</u>
<u>Khumbu</u>	<u>218</u>	<u>563</u>	<u>223605</u>	<u>306729</u>
<u>Lhotse</u>	<u>120</u>	<u>340</u>	<u>94023</u>	<u>170064</u>
<u>Lhotse Nup</u>	<u>29</u>	<u>82</u>	<u>7803</u>	<u>34578</u>
<u>Lhotse Shar</u>	<u>64</u>	<u>242</u>	<u>22626</u>	<u>85770</u>
<u>Nuptse</u>	<u>39</u>	<u>138</u>	<u>45765</u>	<u>66618</u>



**Table S9.** Long-term trends in SGL area on each glacier, as seen in Landsat-derived SGL products. Trends are presented as the lake area change per year from linear regression analysis of the entire timeframe (1988-2022) as well as only for the 2013-2022 period. Results are further broken down by glacier-wide lake area trends near-terminus (lower 50% by distance from terminus) trends. P-values are provided for each.

Glacier	Full Glacier 1988–2022 m <sup>2</sup> yr <sup>-1</sup> (P-value)	Full Glacier 2013–2022 m <sup>2</sup> yr <sup>-1</sup> (P-value)	Terminus only 1988–2022 m <sup>2</sup> yr <sup>-1</sup> (P-value)	Terminus only 2013–2022 m <sup>2</sup> yr <sup>-1</sup> (P-value)
Ama Dablam	<del>156</del> <del>(0.101)</del> <u>128</u> (0.355)	<del>1009</del> <del>(0.064)</del> <u>1156</u> (0.117)	<del>47</del> <del>(0.340)</del> <u>34</u> (0.587)	<del>919</del> <del>(0.029)</del> <u>1143</u> (0.025)
Ambulapcha	<del>239</del> <del>294</del> (0.000)	<del>794</del> <del>(0.071)</del> <u>687</u> (0.204)	<del>178</del> <del>249</del> (0.000)	<del>1034</del> <del>(0.002)</del> <u>1135</u> (0.003)
Imja	<del>46</del> <del>(0.073)</del> <u>109</u> (0.004)	<del>0</del> <del>(1.025)</del> (0.500)	<del>41</del> <del>(0.026)</del> <u>112</u> (0.001)	0 ( <del>1.01</del> 0.000)
Khumbu	<del>2465</del> <del>2413</del> (0.000)	<del>12821</del> <del>(0.000)</del> <u>8348</u> (0.001)	<del>2488</del> <del>2678</del> (0.000)	<del>13497</del> <del>12745</del> (0.000)
Lhotse	<del>754</del> <del>(0.033)</del> <u>192</u> (0.740)	<del>3281</del> <del>(0.118)</del> <u>2212</u> (0.302)	<del>414</del> <del>(0.074)</del> <u>382</u> (0.152)	<del>4876</del> <del>(0.004)</del> <u>5408</u> (0.002)
Lhotse Nup	<del>27</del> <del>(0.551)</del> <u>118</u> (0.107)	<del>27</del> <del>(0.895)</del> <u>104</u> (0.757)	<del>5.67</del> <del>(0.706)</del> <u>15</u> (0.587)	<del>35.45</del> <del>(0.797)</del> <u>155</u> (0.340)
Lhotse Shar	<del>743</del> <del>(0.010)</del> <u>1971</u> (0.001)	<del>1047</del> <del>(0.271)</del> <u>1860</u> (0.194)	<del>102</del> <del>(0.148)</del> <u>258</u> (0.025)	<del>11</del> <del>(0.970)</del> <u>286</u> (0.538)
Nuptse	<del>112</del> <del>(0.213)</del> <u>155</u> (0.227)	<del>431</del> <del>(0.361)</del> <u>674</u> (0.271)	<del>246</del> <del>329</del> (0.000)	<del>821</del> <del>(0.165)</del> <u>1045</u> (0.084)

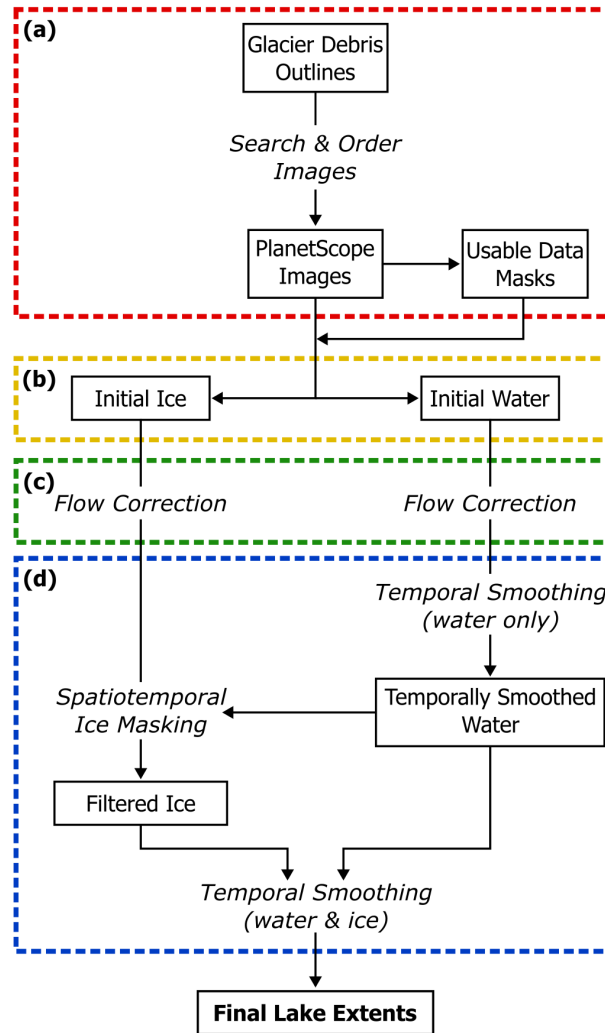


**Figure S1.** Workflow diagram for delineating supraglacial lakes in PlanetScope imagery. The boxed items indicate intermediate products in the workflow, while unboxed, italicized labels indicate processing steps which are referred to in the text.

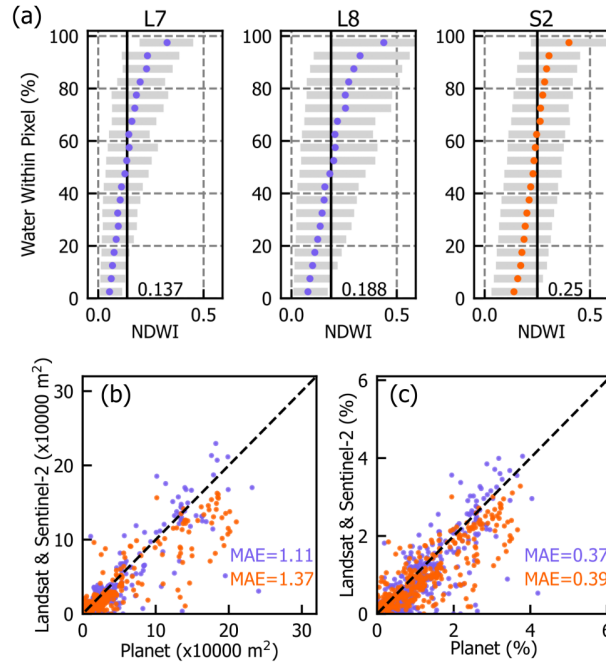


**Figure S2.** (a) NDWI optimization results for each satellite. Each horizontal bar shows the range of NDWI values for Landsat and Sentinel-2 pixels in the validation dataset with the indicated percent water cover (aggregated in 5% bins). Dots indicate the mean, grey bars show the range containing 90% of all observations. Vertical lines and the shown number indicate the optimized NDWI value for each sensor, which minimized the net error over the validation dataset. (b) and (c) compare the SGL area identified in PlanetScope imagery and in Landsat/Sentinel-2 coincident imagery using the optimized thresholds, with each point representing a single image. (b) shows these values as the total lake area, while (c) scales them by the total glacier debris-covered area. Mean absolute error (MAE) is shown for Landsat (purple) and Sentinel-2 (orange) results on each plot.

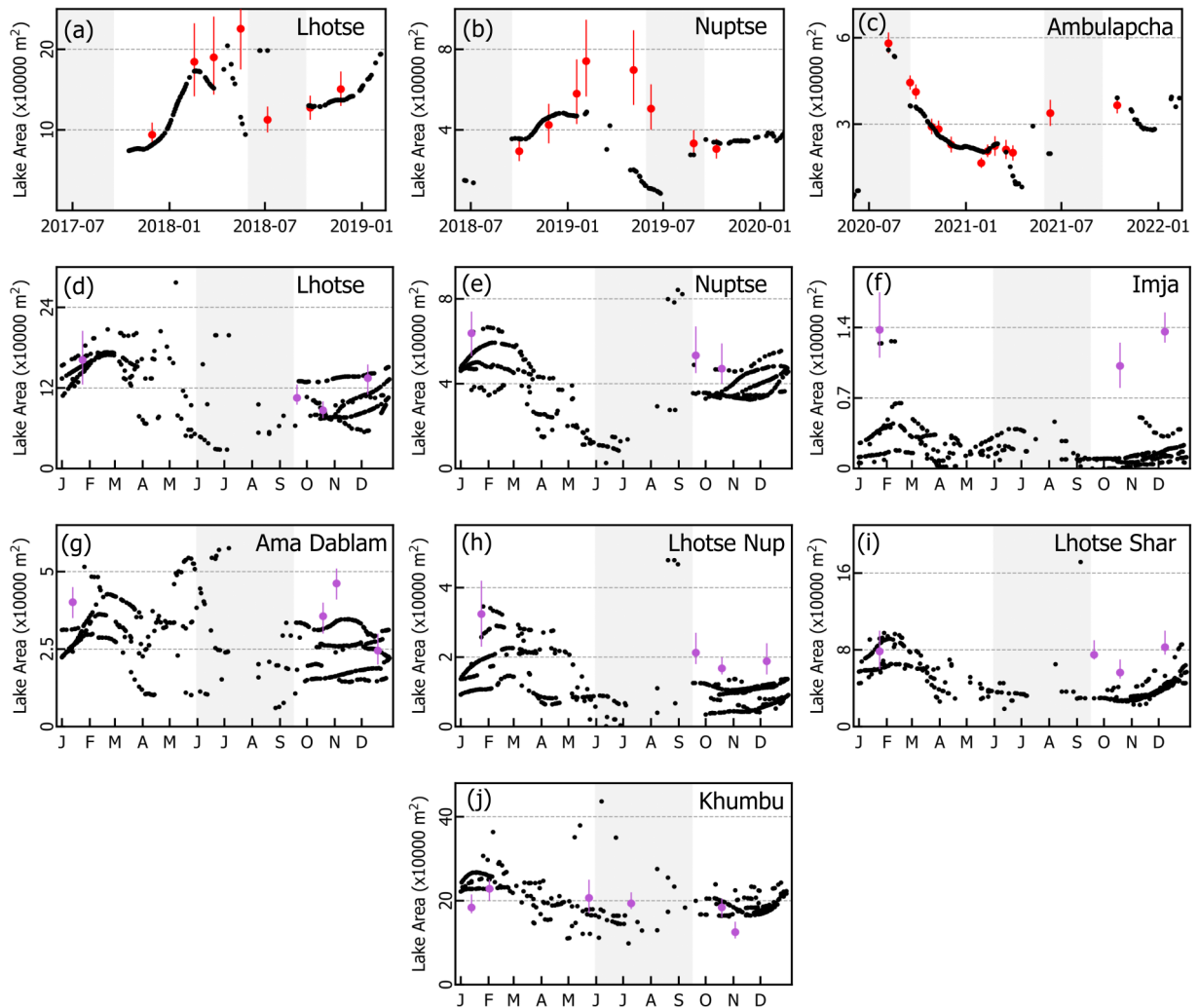


**Figure S3.** a-c) A comparison of automated lake areas (black dots) to the manually-delineated validation images on Lhotse, Nuptse, and Ambulapcha Glaciers (red). d-j) Comparison between automated lake areas and results from Watson et al. (2016, purple). Comparisons with Watson et al. are presented with results plotted by day of year (tick labels indicating the beginning of each month), as there was no temporal overlap between our observations and theirs. Grey shaded areas indicate monsoon months. Red and purple bars indicate error estimates from a  $\pm 1$  pixel buffering.

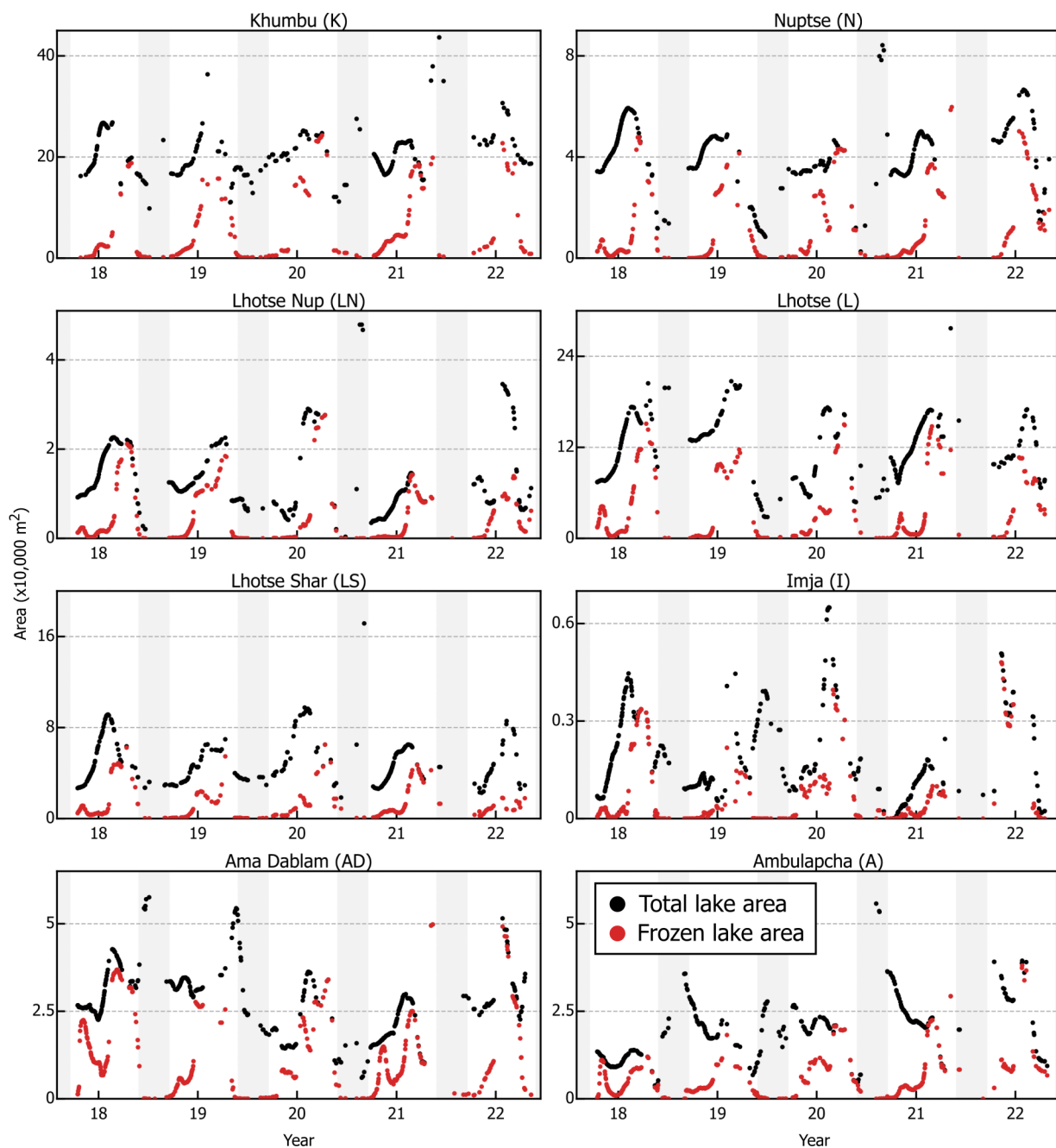


**Figure S4.** Comparison of the timeseries of total lake area (black points) and the total area of lake surface which are frozen (red points) for each glacier across the five-year study period.

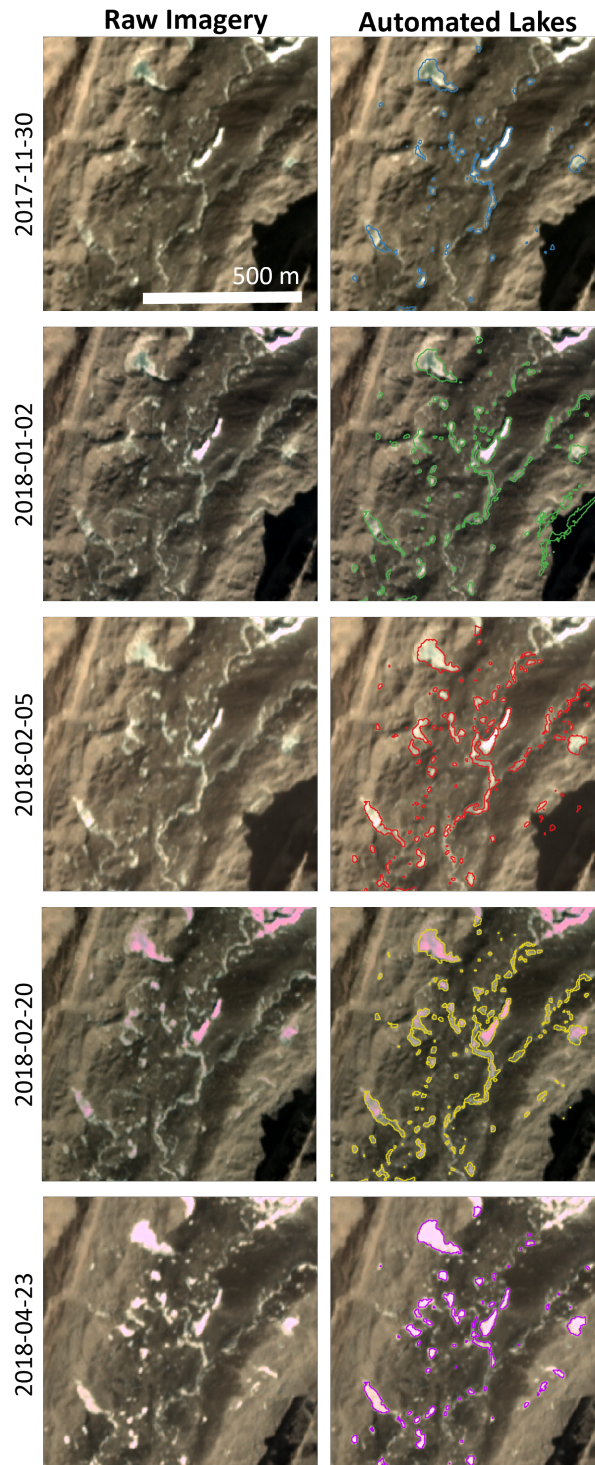


**Figure S5.** An example of the SGL changes in the upper region of Khumbu Glacier between November 2017 and April 2018. Outlines show the automated SGL identification.



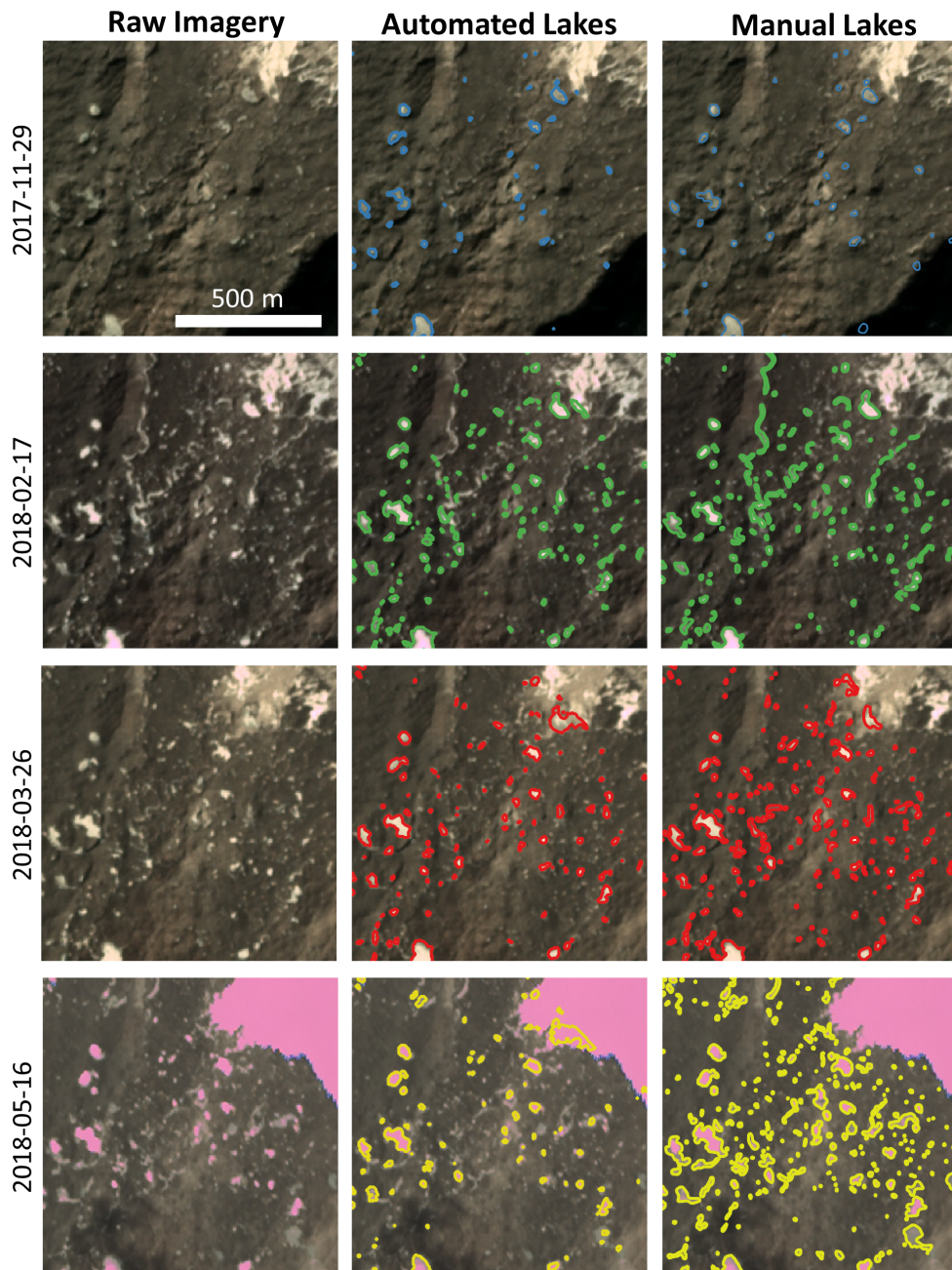


**Figure S6.** An example of the SGL changes in the upper region of Lhotse Glacier between November 2017 and May 2018. Center outlines show the automated SGL identification, left outlines show the manual validation dataset outlines.



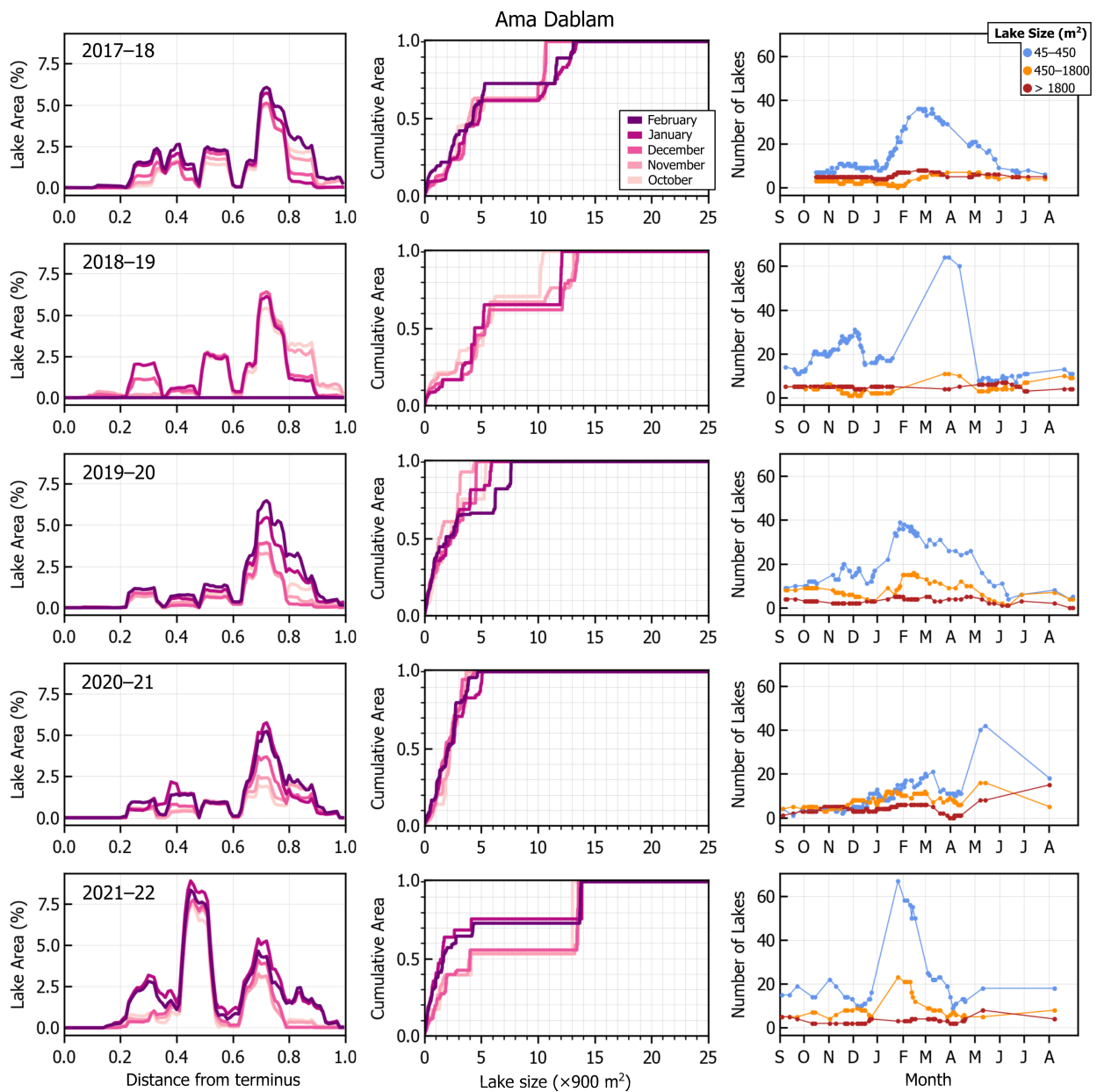


**Figure S7.** Seasonality in lake area and count on Ama Dablam Glacier, presented identically as Figure 40-6.

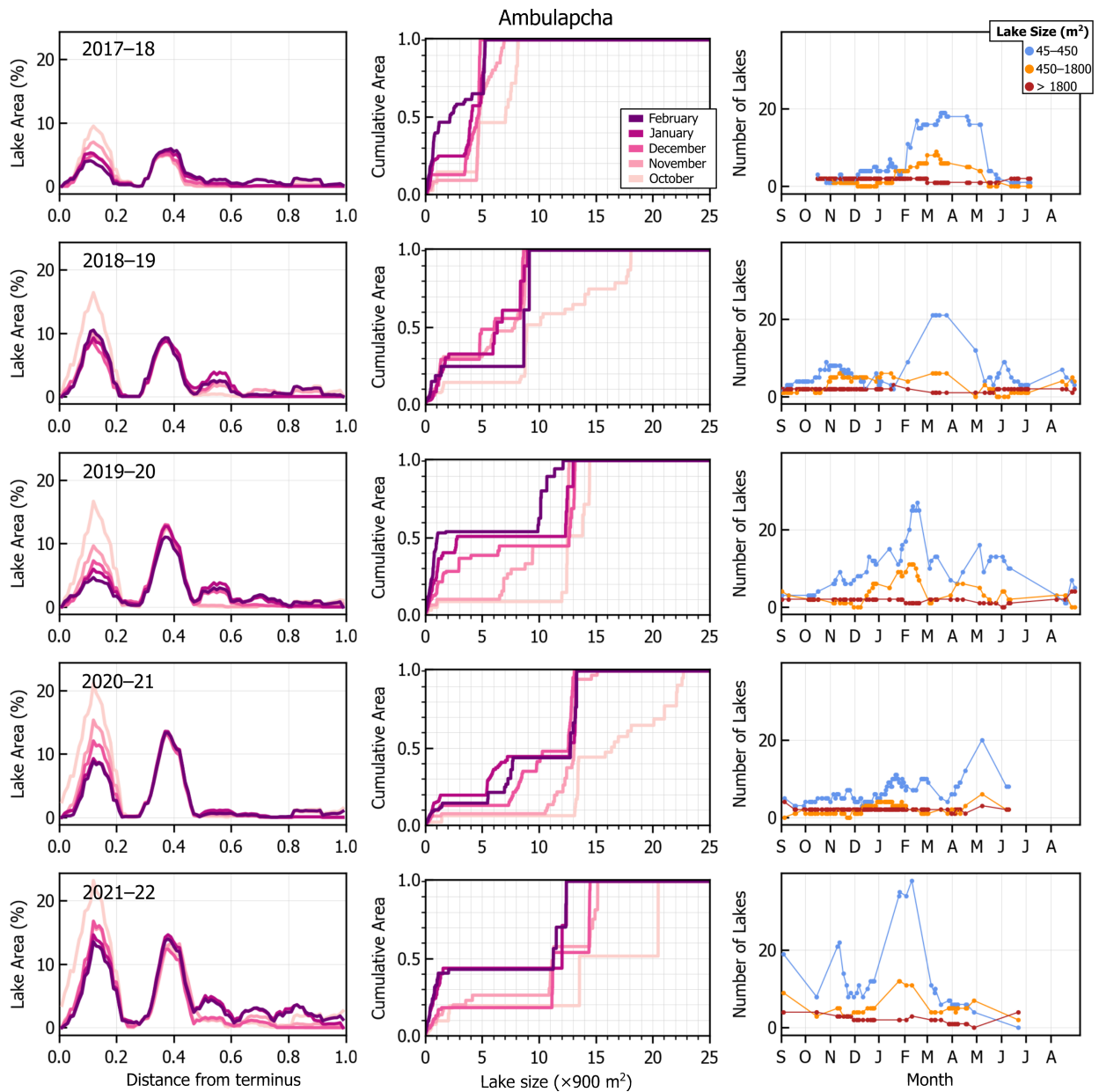


**Figure S8.** Seasonality in lake area and count on Ambulapcha Glacier, presented identically as Figure 10-6.

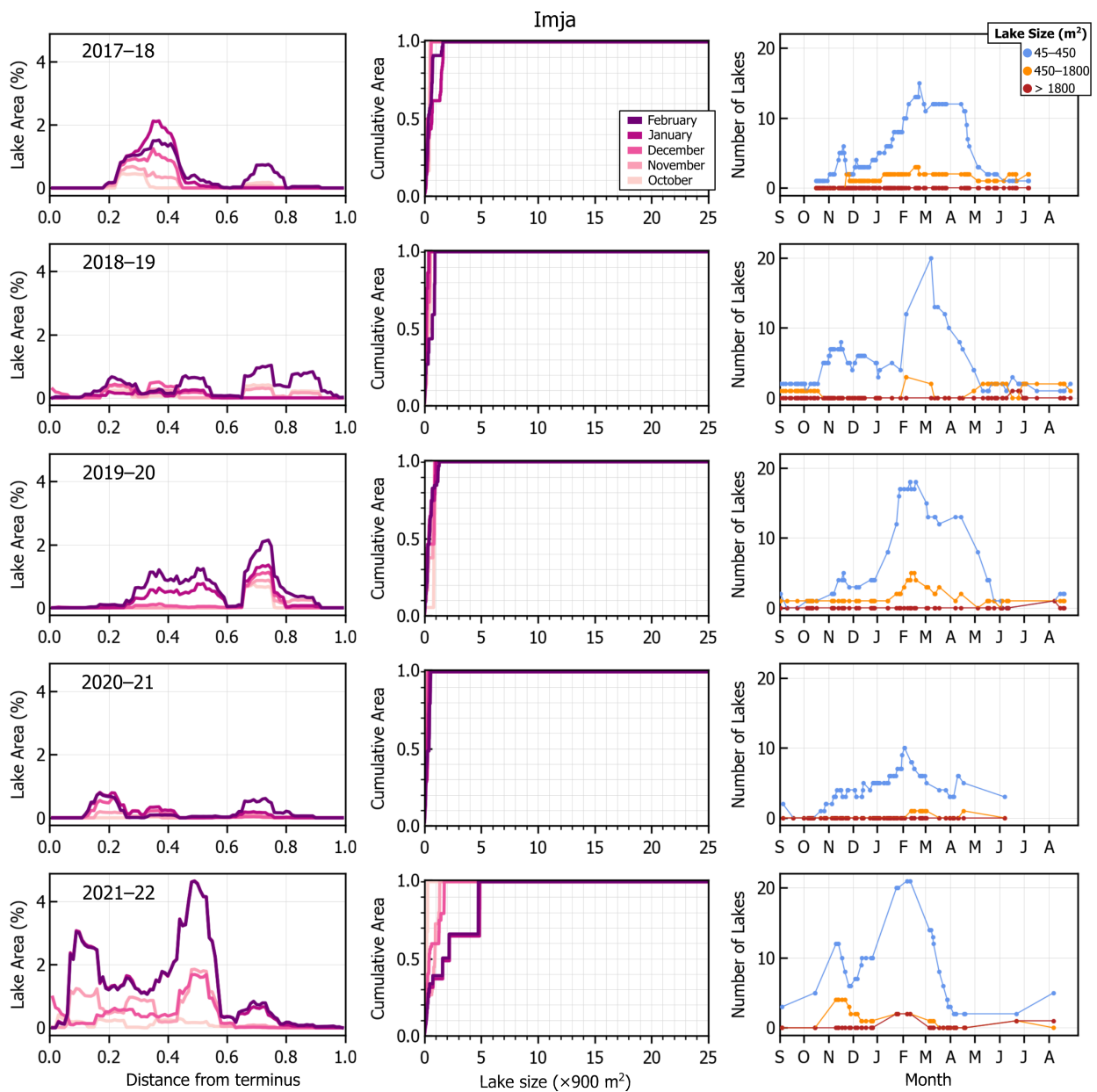


**Figure S9.** Seasonality in lake area and count on Imja Glacier, presented identically as Figure 10-6.

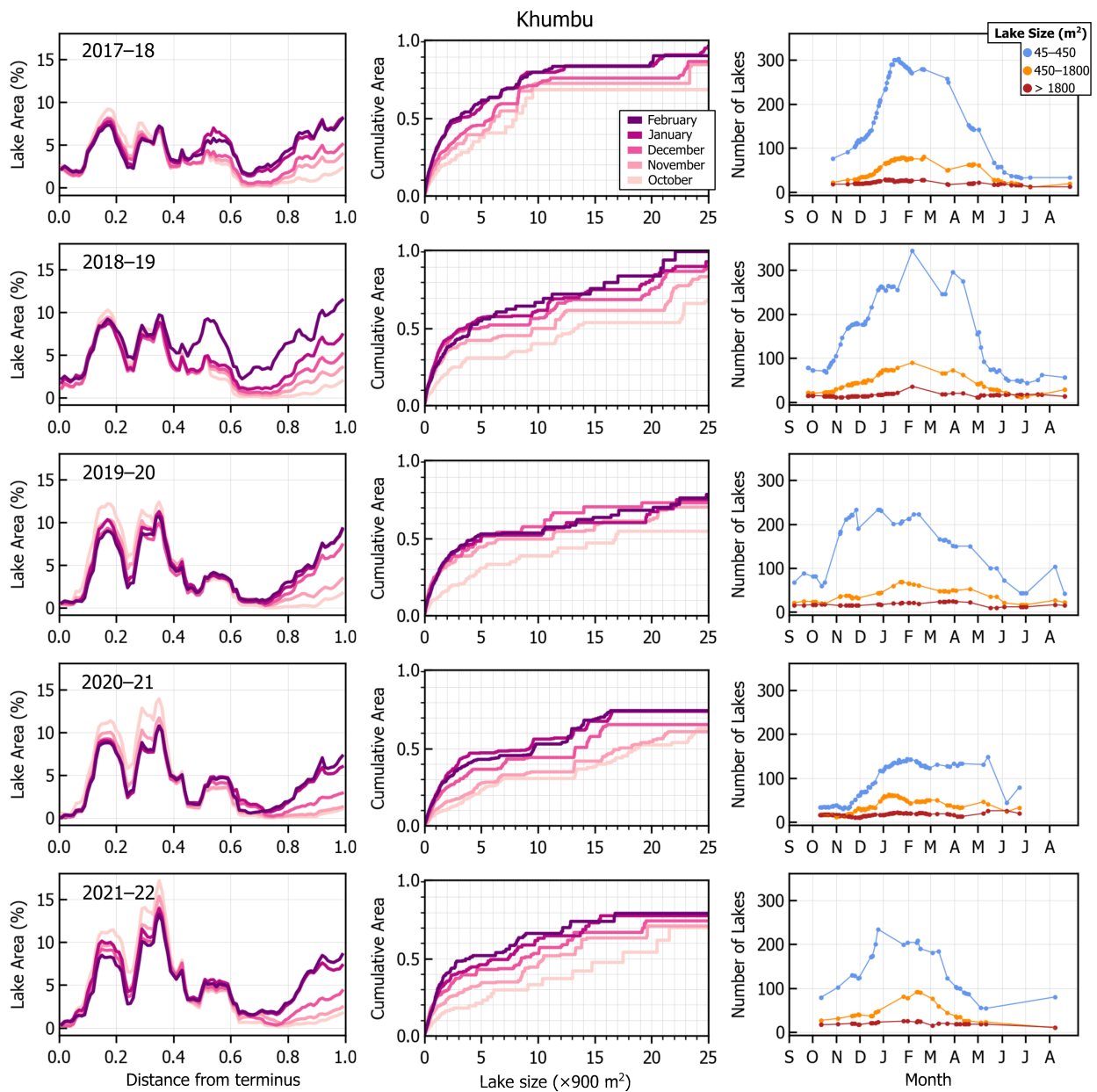


**Figure S10.** Seasonality in lake area and count on Khumbu Glacier, presented identically as Figure 40-6.

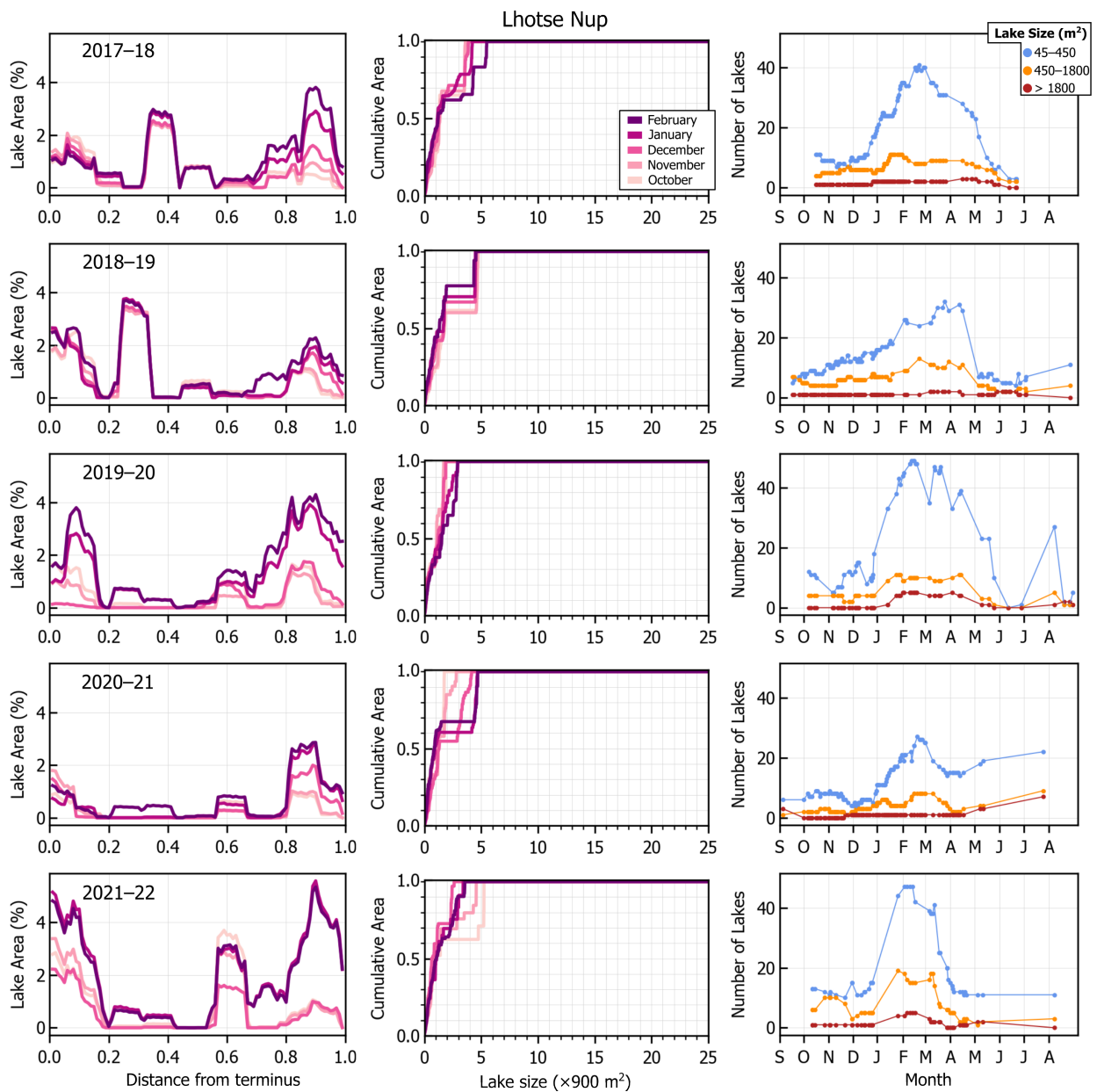


**Figure S11.** Seasonality in lake area and count on Lhotse Nup Glacier, presented identically as Figure 10-6.

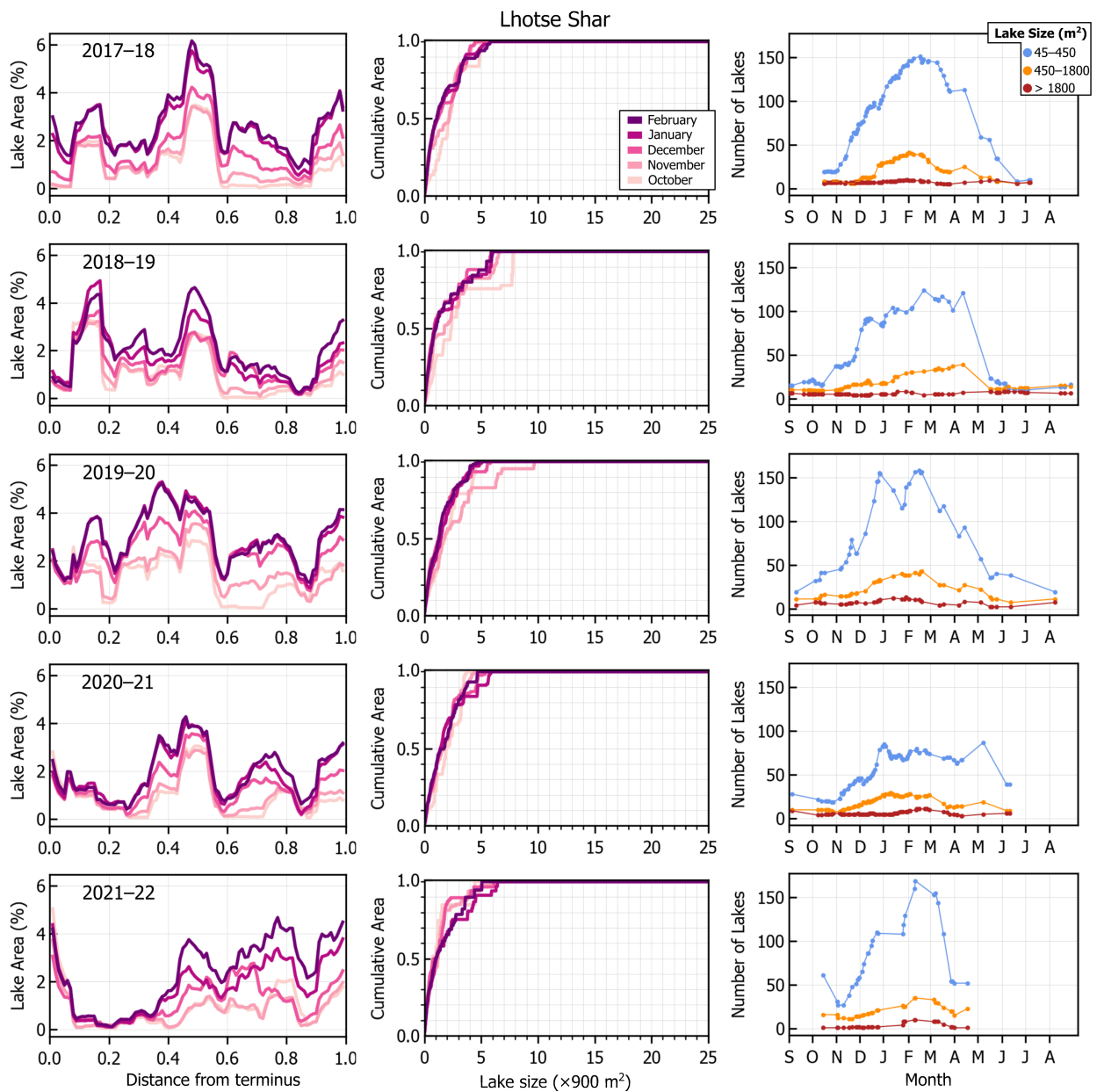


**Figure S12.** Seasonality in lake area and count on Lhotse Shar Glacier, presented identically as Figure 40-6.

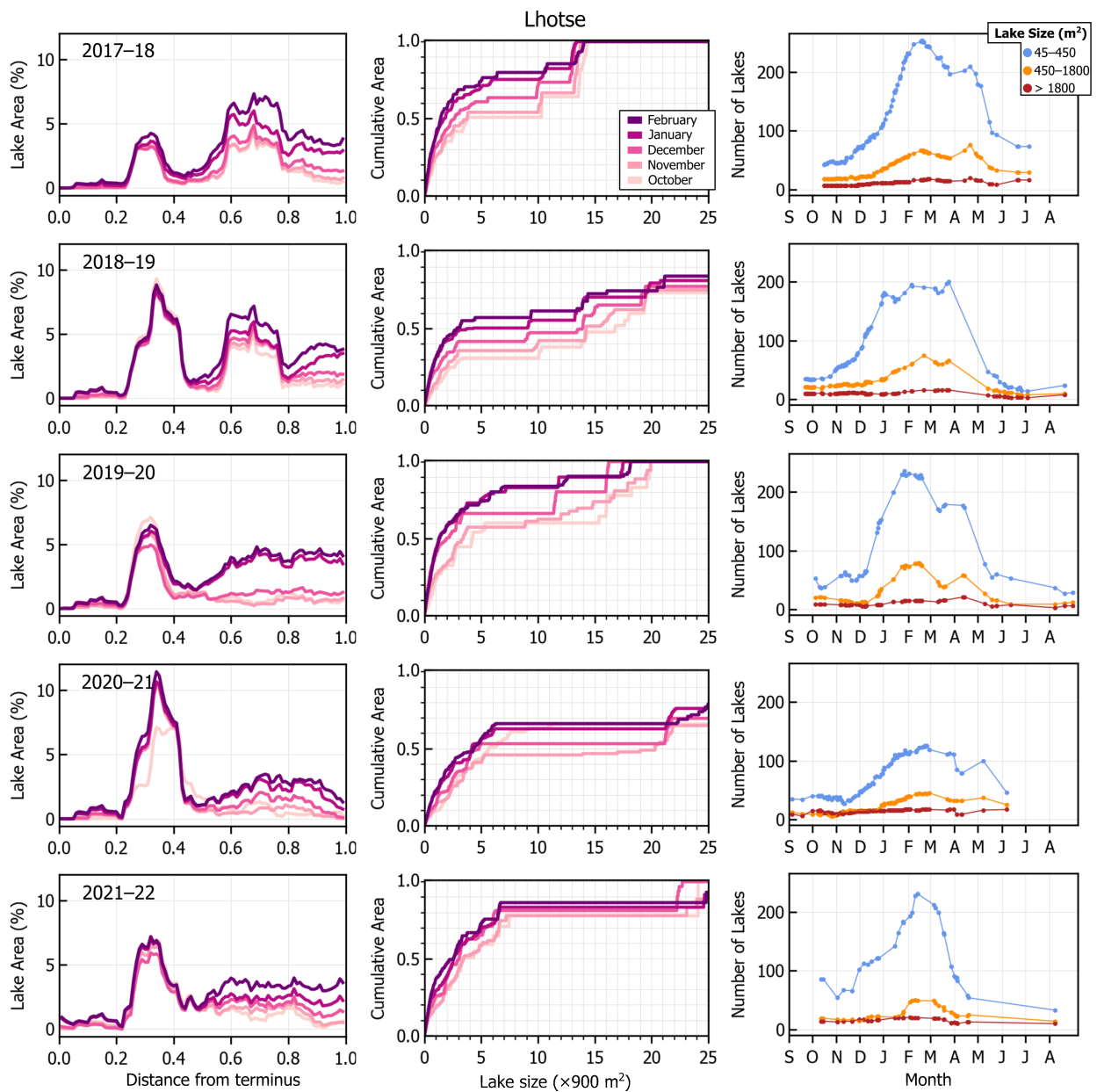


**Figure S13.** Seasonality in lake area and count on Lhotse Glacier, presented identically as Figure 10-6.



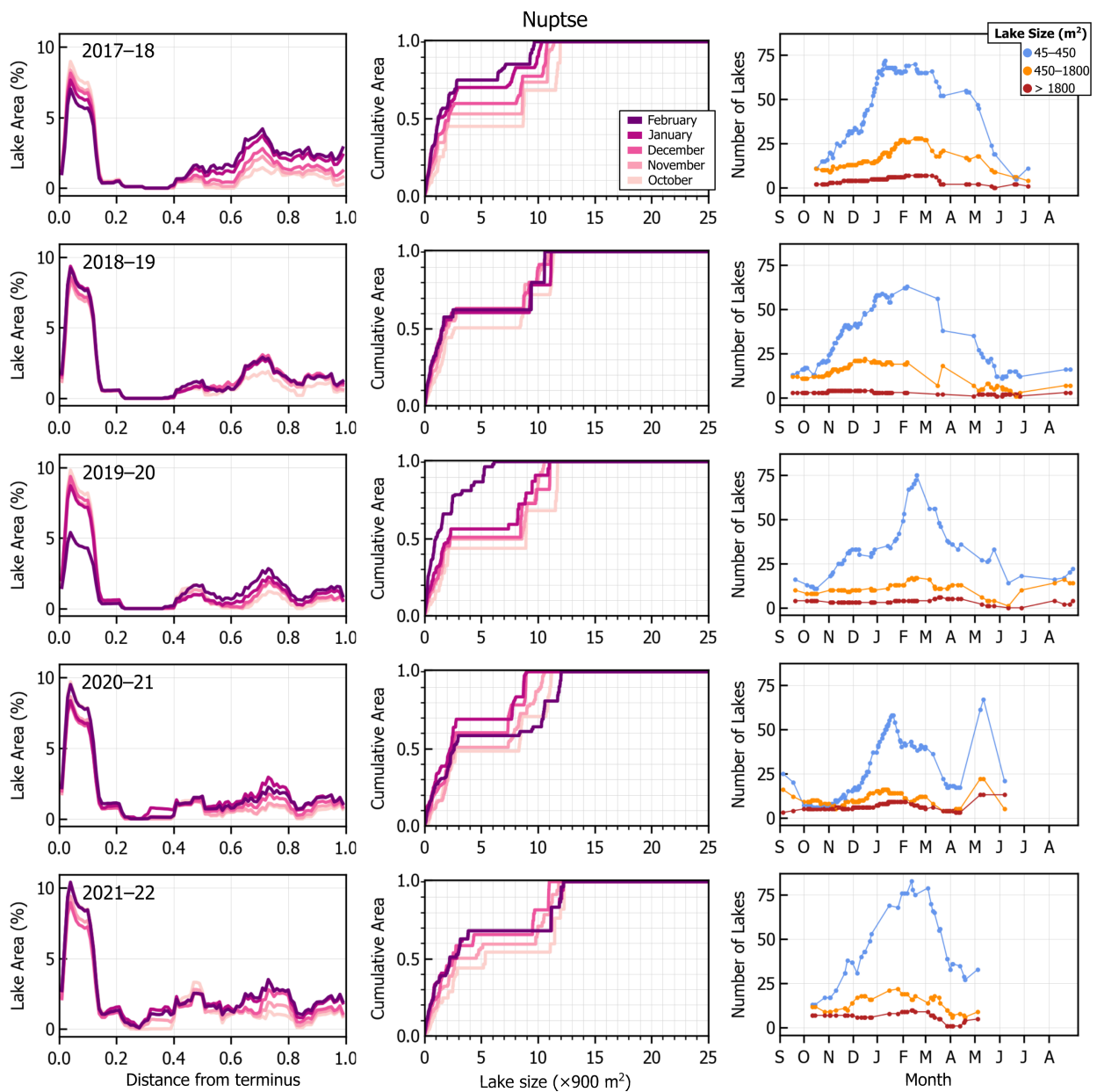


**Figure S14.** Seasonality in lake area and count on Nuptse Glacier, presented identically as Figure 10-6.

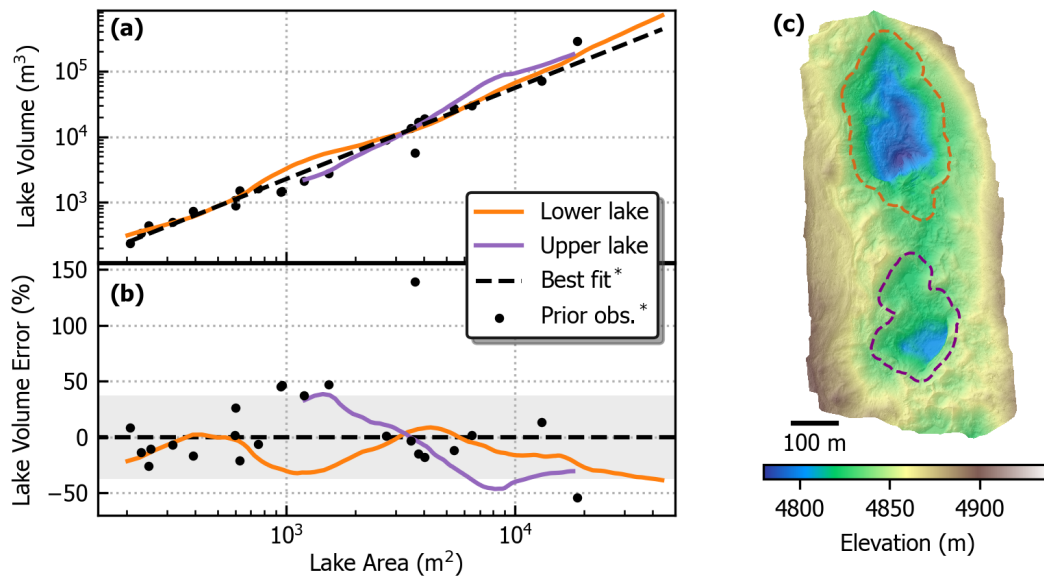


**Figure S15.** ~~Seasonality of~~ The area-volume scaling relationship for the two large lake basins on Ambulapcha Glacier (purple and orange lines). Black points show previous observations of SGL areas and volumes on Khumbu Glacier by Watson et al. (2018b), ~~near-terminus lakes~~ and the black dashed line is the best-fit relationship presented in the study. ~~Defined as lakes-~~(a) shows the area-volume relationship (in log-log scale). (b) shows the ~~lower half of~~ percent error that results from using the ~~debris-covered~~ best-fit equation for estimating volume from an observed area, with maximum extents greater than or equal to 3 Landsat pixels. Grey shaded area shows the 37% mean error from all observations in Watson et al. (2700-m<sup>2</sup>2018b). (c) shows the UAS-derived DEM (hillshade with elevation overlaid) and approximate extents of the two lake basins.

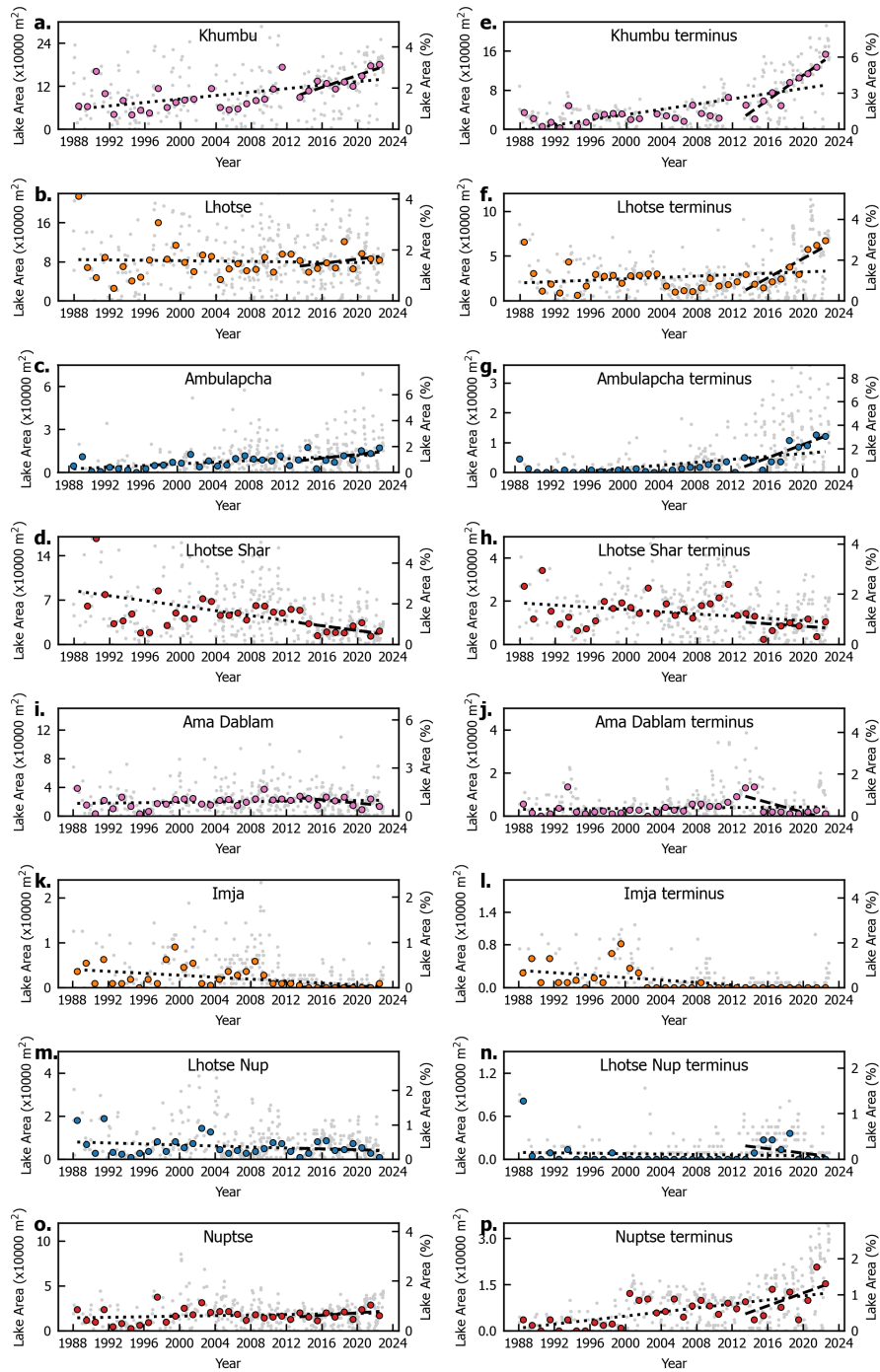


**Figure S16.** Landsat-derived time series of SGL area of all 8 glaciers.

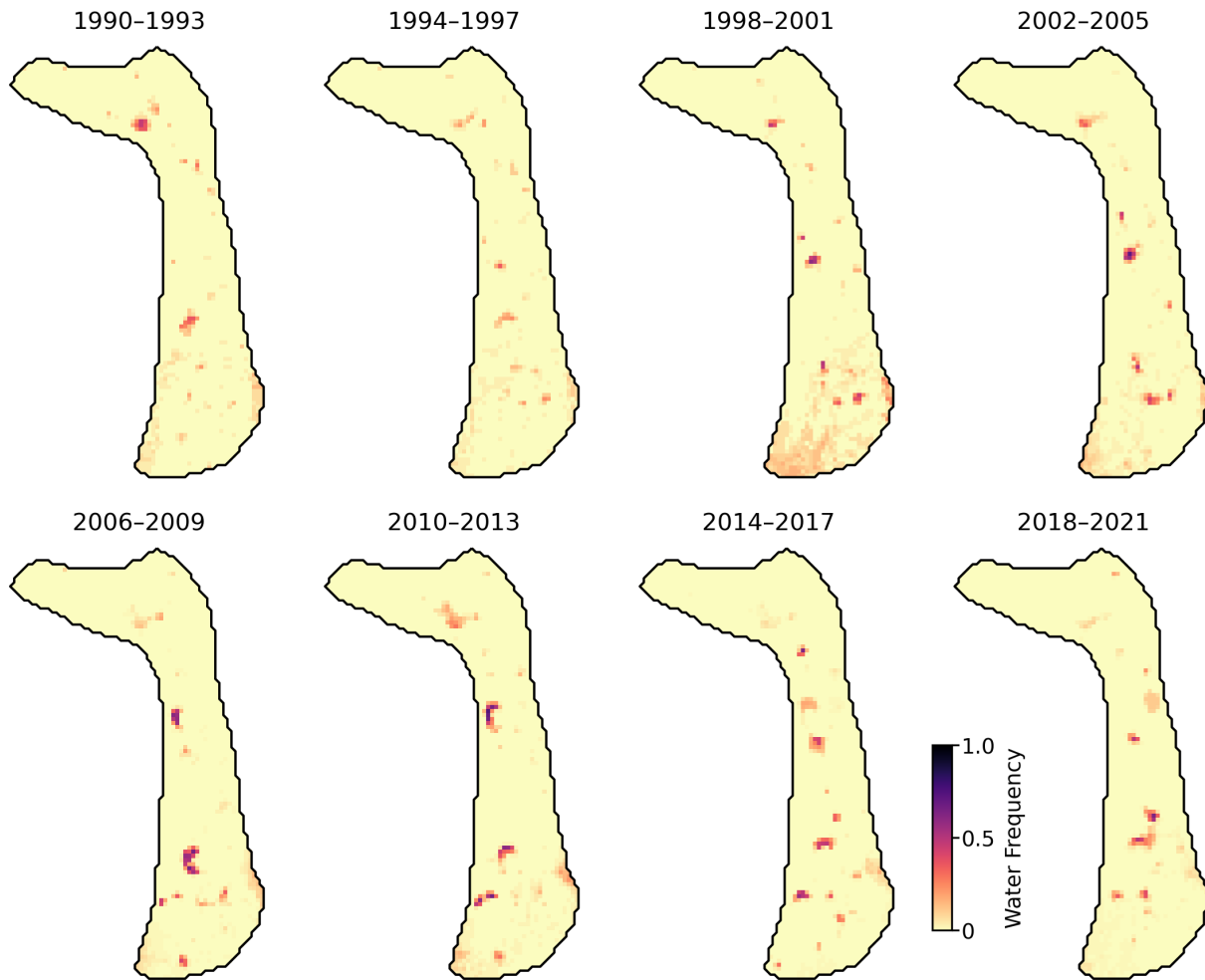


**Figure S17.** Repeat 4-year maps of SGLs on Ama Dablam Glacier, from Landsat imagery.

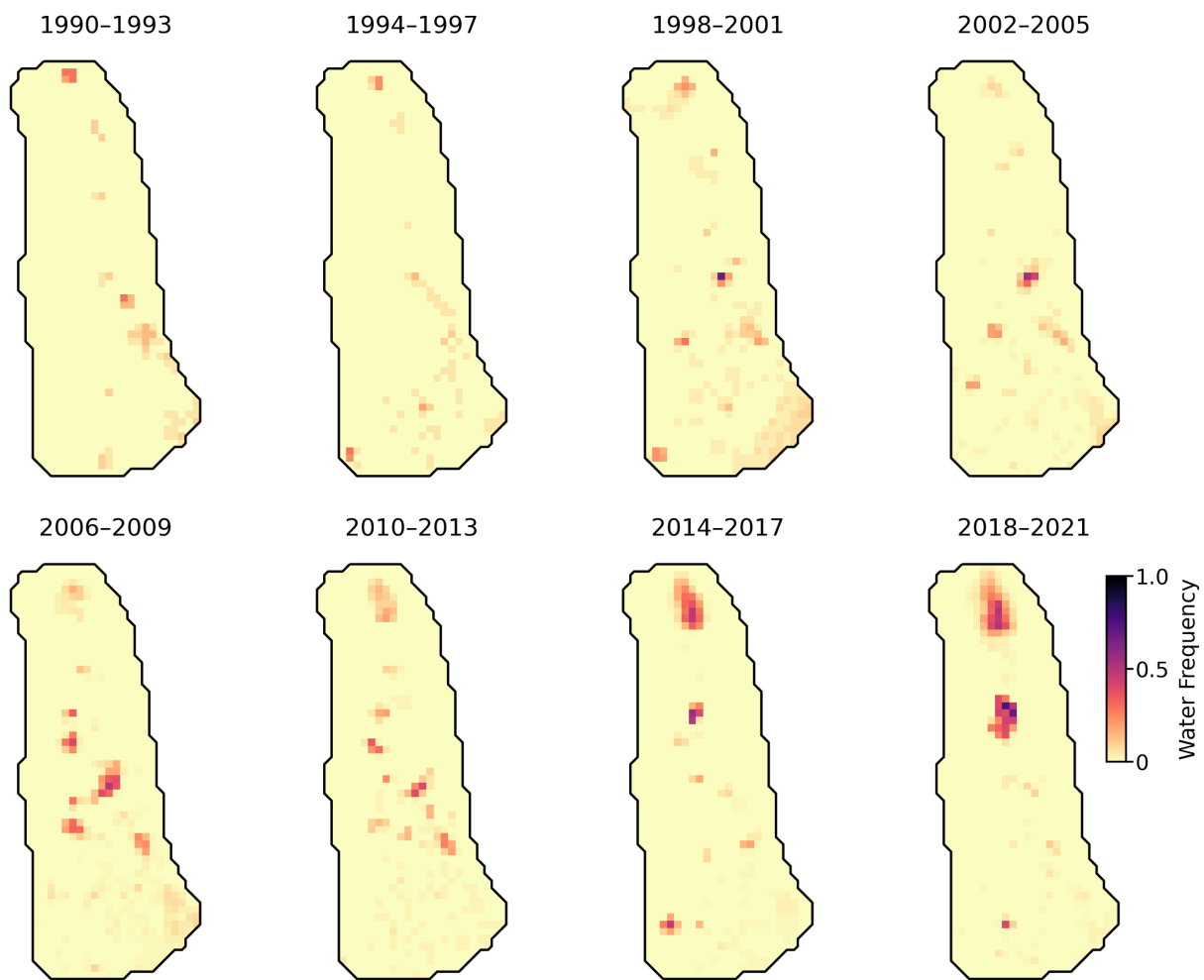
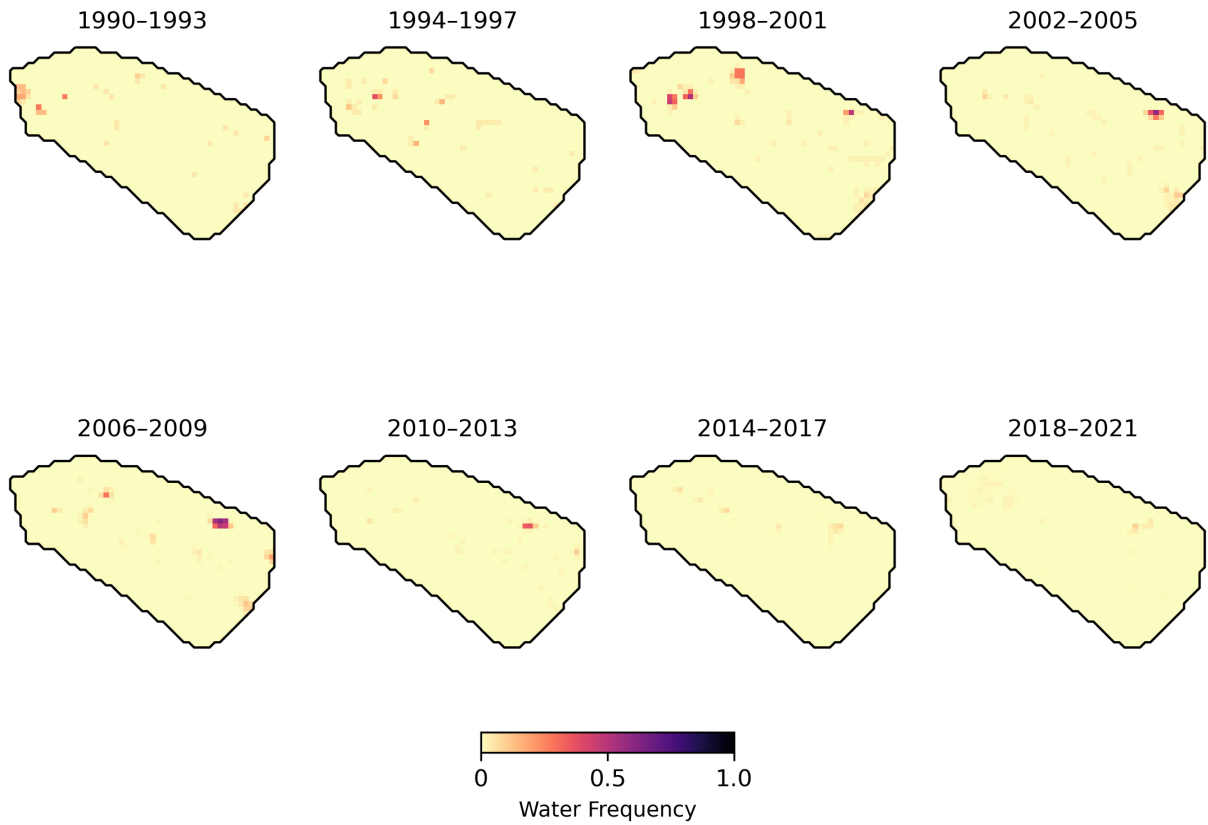


**Figure S18.** Repeat 4-year maps of SGLs on Ambulapcha Glacier, from Landsat imagery.

Repeat 4-year maps of SGLs on Imja Glacier, from Landsat



imagery:

Figure S19. [Repeat 4-year maps of SGLs on Imja Glacier, from Landsat imagery.](#)

Repeat 4-year maps of SGLs on Lhotse Nup Glacier, from Landsat imagery.

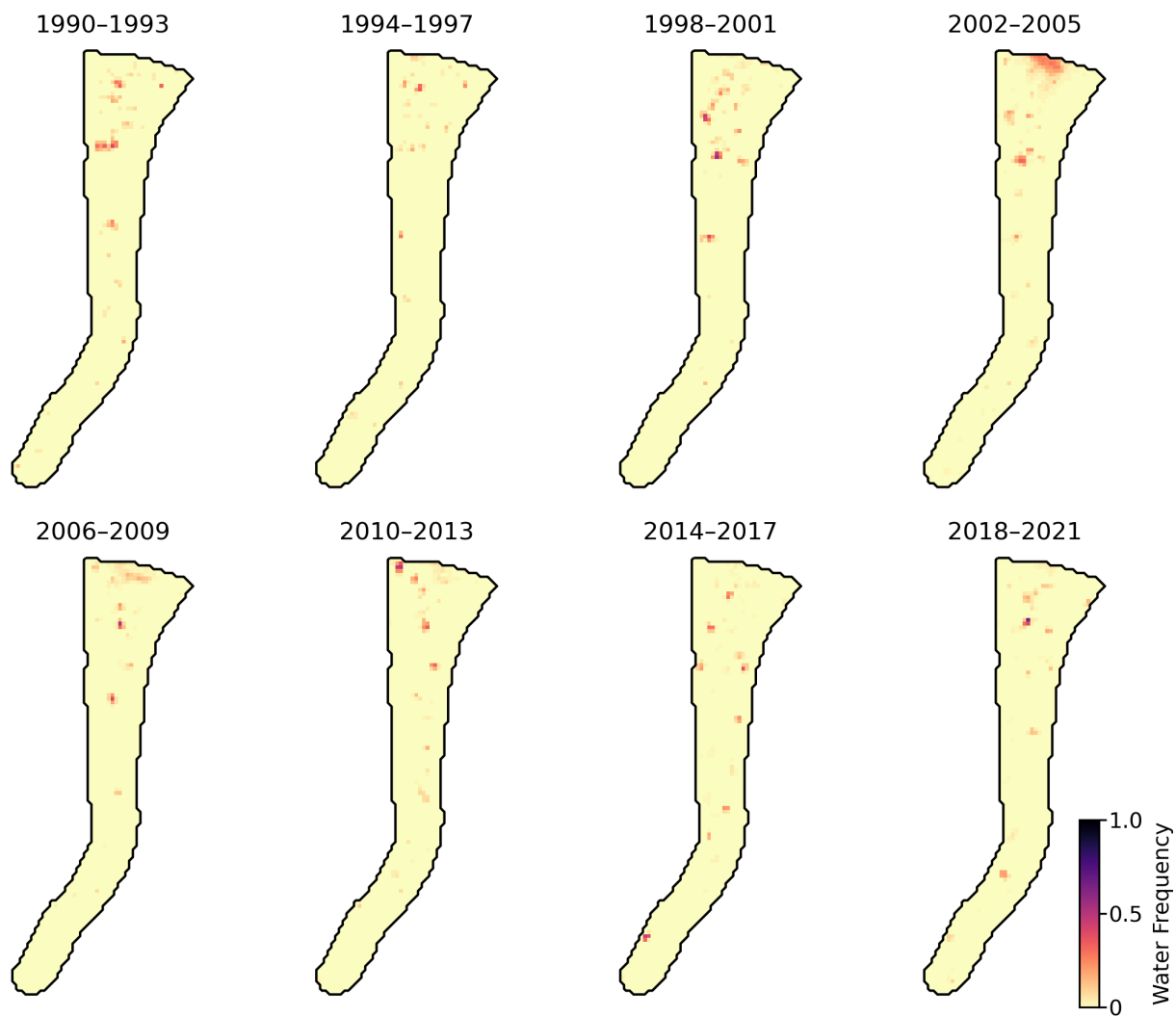


Figure S20. Repeat 4-year maps of SGLs on Lhotse Nup Glacier, from Landsat imagery.



Repeat 4-year maps of SGLs on Lhotse Shar Glacier, from Landsat imagery.

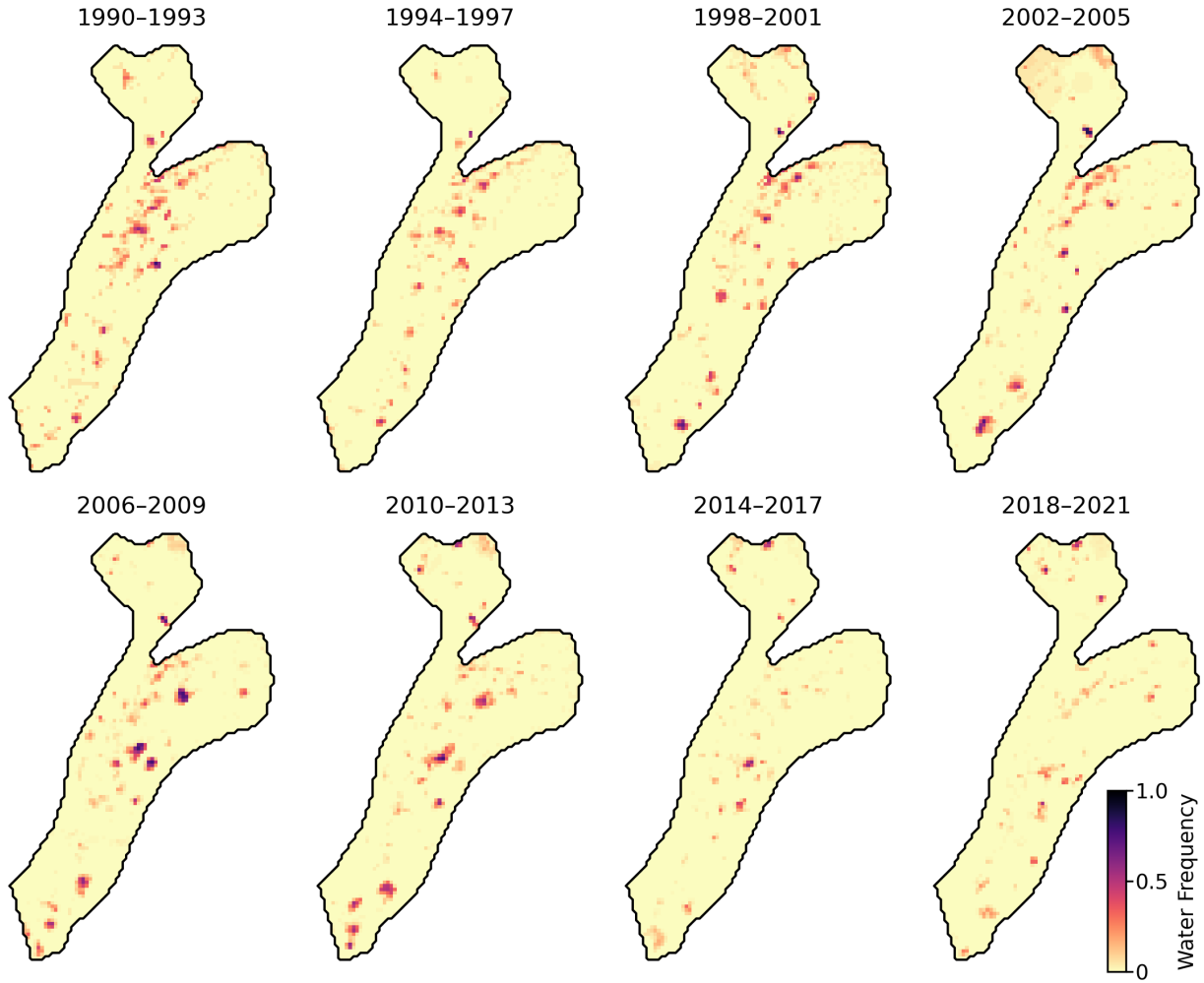


Figure S21. [Repeat 4-year maps of SGLs on Lhotse Shar Glacier, from Landsat imagery.](#)

Repeat 4-year maps of SGLs on Lhotse Glacier, from Landsat imagery.

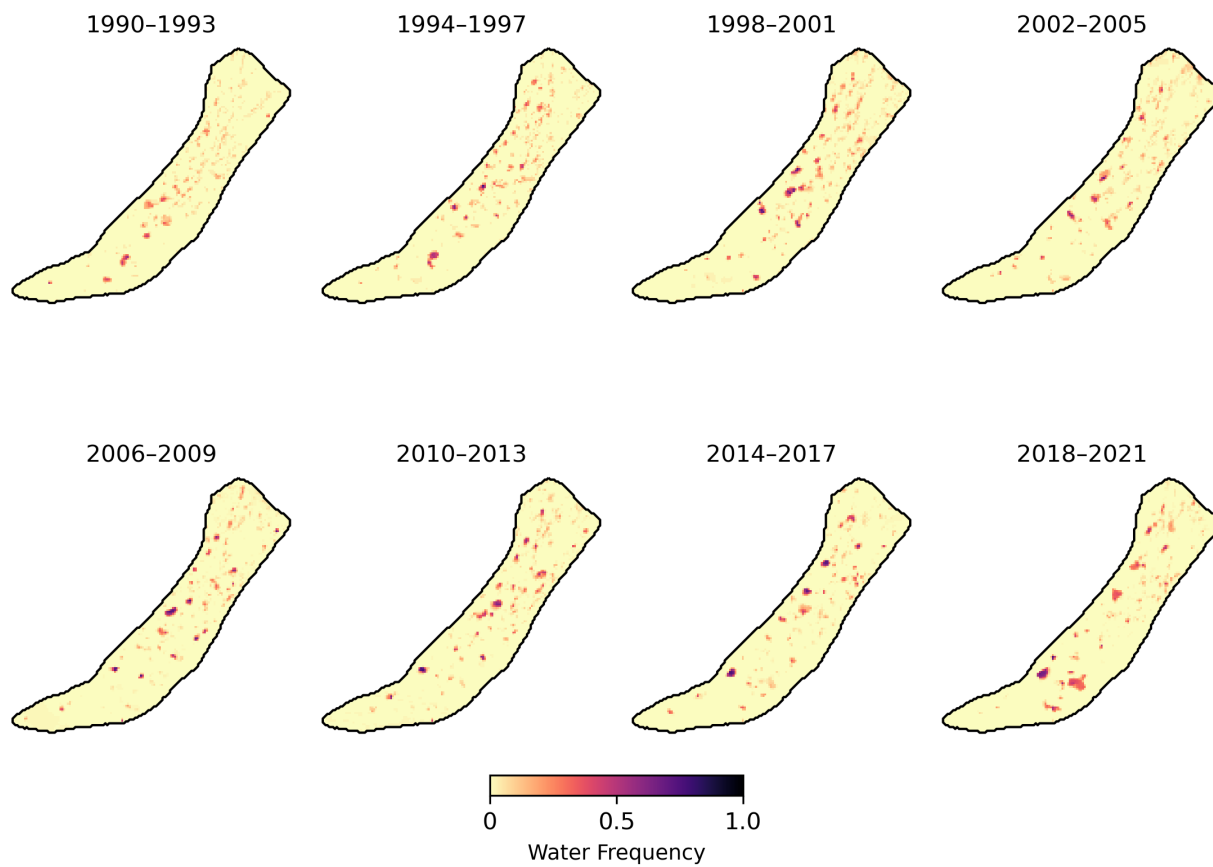
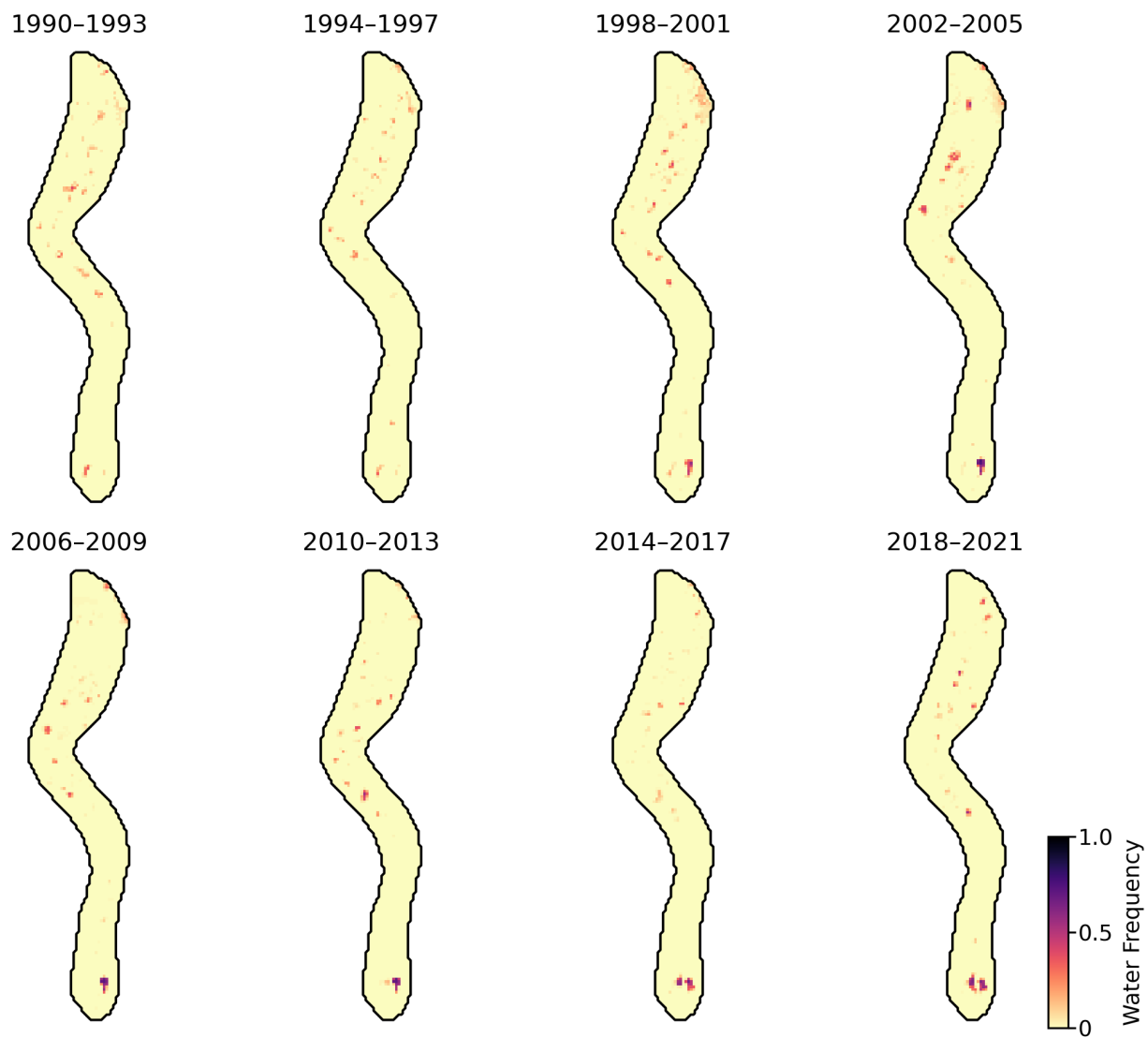


Figure S22. [Repeat 4-year maps of SGLs on Lhotse Glacier, from Landsat imagery.](#)



**Figure S23.** Repeat 4-year maps of SGLs on Nuptse Glacier, from Landsat imagery.